minerals

MDPI

Article

Petrology and Geochemistry of Mesoarchean Sukinda Ultramafics, Southern Singhbhum Odisha Craton, India: Implications for Mantle Resources and the Geodynamic Setting

Debajyoti Nayak [1], Pranab Das [1,*] and Sagar Misra [2]

[1] Department of Applied Geology, Indian Institute of Technology (Indian School of Mines), Dhanbad 826004, India; 16dr000219@iitism.ac.in
[2] Department of Applied Geology, National Institute of Technology Raipur, Chhattisgarh 492010, India; smisra.geo@nitrr.ac.in
* Correspondence: pranab@iitism.ac.in; Tel.: +91-947-119-1892

Abstract: The Sukinda ultramafic complex in India comprises precisely two areas: Kaliapani (KLPN) and Katpal (KTPL). These areas consist of a sequence of lithotypes, including orthopyroxenite, dunite, serpentinite, and chromitite, displaying a rhythmic layering of rocks. These rocks exhibit a cumulate texture and stand out due to their elevated Mg# (78.43–93.20), Cr (905.40–58,799 ppm), Ni (193.81–2790 ppm), Al_2O_3/TiO_2 (27.01–74.06), and Zr/Hf (39.81–55.24) ratios, while possessing lower TiO_2 contents (0.01–0.12 wt%). These ultramafics, characterized by low Ti/V (0.83–19.23) and Ti/Sc (7.14–83.72) ratios, negative anomalies of Zr, Hf, Nb, and Ti in a primitive mantle-normalized spider diagram, indicate that the ultramafics originate from a depleted mantle source. Furthermore, the presence of enriched LREE compared to HREE, a negative Eu anomaly, and enrichment of Th, U, and negative Nb anomalies suggest a subduction setting. The whole-rock geochemical data reveal high levels of MgO, Cr, and Ni, as well as low TiO_2 and CaO/Al_2O_3 ratios and high Al_2O_3/TiO_2 ratios. Moreover, the mineral chemistry data of the ultramafic rocks show high-Mg olivine (Fo 90.9−94.1) in dunite, high-Mg orthopyroxene (En 90.4–90.7) in orthopyroxenite, and high Cr# (0.68–0.82) and low Mg# (0.40–0.54) in chromite, alongside significant Al_2O_3 (9.93–12.86 wt%) and TiO_2 (0.20–0.44 wt%) contents in the melt. Such geochemical characteristics strongly suggest that the Sukinda ultramafic originates from the fractional crystallization of a boninitic parental magma, which is derived from the second-stage melting in a depleted metasomatized mantle source within a supra-subduction zone tectonic setting.

Keywords: boninites; chromites; Singhbhum Craton; Sukinda ultramafic complex; supra-subduction zone

Citation: Nayak, D.; Das, P.; Misra, S. Petrology and Geochemistry of Mesoarchean Sukinda Ultramafics, Southern Singhbhum Odisha Craton, India: Implications for Mantle Resources and the Geodynamic Setting. *Minerals* **2023**, *13*, 1440. https://doi.org/10.3390/min13111440

Academic Editor: Federica Zaccarini

Received: 18 July 2023
Revised: 19 September 2023
Accepted: 26 September 2023
Published: 14 November 2023

1. Introduction

Mafic and ultramafic rock formations have proven to be significant hosts for precious mineral deposits, including chromium minerals (chromites), nickel–copper sulfides, iron oxides, and elements from the platinum group (PGEs) [1]. Chromite deposits, known as chromites, have experienced mineralization from the Precambrian to the Phanerozoic era, with notable occurrences in Mesoarchean times. These chromite deposits are frequently located within sill-shaped ultramafic rock formations in greenstone belts across diverse regions of the globe. Some notable examples of Archean chromiferous layered sill-like ultramafic provinces include the Kaapvaal Craton [2] and Bushveld Layered Igneous intrusion in South Africa [3], Emeishan Large Igneous Province in southwest China [4,5], Zimbabwe Craton [6–8], and the Singhbhum and Dharwar Cratons of the Indian shield [9,10].

Chromiferous ultramafic deposits are found in the Singhbhum Craton (Sukinda–Nuasahi–Jojohatu area) and Dharwar Craton (Nuggihalli–Krishnarajpet–Holenarsipur–Nagamangala–Javanhalli area) within the Indian shield. These deposits occur as sill-like ultramafic deposits within Archean greenstone belts [9–14]. They are genetically associated

with high-Mg lithotypes, such as komatiites, komatiitic basalts, siliceous high-Mg basalts (SHMBs), picrites, and boninites [10,15]. Significant chromiferous layered ultramafic rocks are accommodated within the Archaean greenstone belt in the Singhbhum Craton [10,16]. The Nuasahi and Sukinda areas of the Odisha state and the Roro–Jojohatu area of Jharkhand state host significant ultramafic–mafic igneous complexes that intrude into the iron ore group [17–19]. The largest ultramafic body in the Singhbhum Craton is the Sukinda massif, a layered complex composed of rhythmic layers of orthopyroxenite–dunite–serpentinite–chromitite. The Sukinda ultramafic complex has intruded into the Archaean iron ore group (IOG) of rocks (cherty quartzite and banded magnetite quartzite) in the Singhbhum Craton. It has intruded at a width of 2–5 km and extends nearly 25 km in an ENE–WNW direction from Kansa (east) to Maruabil (west) and beyond [10]. In order to conduct a comprehensive study of the Sukinda ultramafic complex, rock samples were collected from two distinct regions: Kaliapani (KLPN) and Katpal (KTPL).

Previous studies of the Sukinda ultramafic complex have focused on the chromite mineralization associated with ultramafics [10,20–22] and suggested that the Sukinda ultramafics are part of an Archean ophiolite complex based on a limited platinum-group element (PGE) analysis. Ref. [16] stated that the chromiferous ultramafic cumulates of Sukinda are part of the conformable and tectonically overlying Archean greenstone sequence and can be compared to the present-day oceanic crust. However, based on chromite chemistry, Ref. [10] proposes that the Sukinda ultramafics are formed from boninitic or siliceous high-Mg basalts in a supra-subduction zone setting.

However, limited efforts have been dedicated to investigating the comprehensive chemical composition of whole rocks and individual minerals within the Katpal and Kaliapani regions of the Sukinda ultramafic complex. This study focuses on scrutinizing the characteristics of Sukinda ultramafic rocks and the associated minerals. It aims to present insights into the origin and evolutionary history of the Sukinda ultramafic complex. By analyzing the geochemical datasets and mineral makeup of the rocks in these specific areas, a more comprehensive understanding of the evolution of the Earth's crust during the Archaean period and its geographical interrelationships will emerge. Achieving an improved comprehension of the geological conditions in which ultramafic rocks hosting chromite were formed offers valuable insights for future explorations of chromite and platinum deposits within the Archaean greenstone belts.

2. Geological Setting

2.1. Regional Geology

The Indian shield consists of five Archean cratonic nuclei, i.e., the Singhbhum Odisha Craton (SOC), Baster Craton, Dharwar Craton, Aravali Craton, and Bundelkhand Craton. The Sukinda ultramafic complex (present study area) is accommodated within the Singhbhum Odisha Craton. The SOC, composed of Archaean–Palaeoproterozoic rocks, spreads over 40,000 km^2 in the Singhbhum district (Jharkhand) and the northern part of the Odisha state (Figure 1a) having (1) a supra-crustal sequence of an older metamorphic group (OMG) and older metamorphic tonalitic gneiss (OMTG); (2) different phases of granitoid batholiths (e.g., Singhbhum granite, Nilgiri granite, Bonai granite, Chakradharpur granite–gneiss, and Mayurbhanj granite); (3) younger supra-crustals of the iron ore group (IOG), which accommodates a banded iron formation (BIF) of economic interest; and (4) the SOC also contains basic volcanic formations (i.e., Simlipal, Dhanjori, and Dalma), and some mafic-ultramafic complexes, i.e., the Baula–Nuasahi and Sukinda ultramafic complex, Mayurbhanj gabbro–anorthosite complex, and newer mafic dolerite dyke swarms. The oldest recognizable litho-unit of the Singhbhum Orissa Craton (SOC) is the OMG, dated using zircon U-Pb at 3500 Ma [23]. The OMG is exposed in the Keonjhar district, west of the Champua areas [24]. The lithology of the OMG comprises various types of rocks, such as pelitic schists, quartz–magnetite–cummingtonite schists, quartzites, banded calc-gneiss, and ortho and para-amphibolites [25]. An intrusion in the OMG rocks led to the formation of the OMTG, which led to the formation of the OMTG, which is predominantly

tonalitic–trondhjemitic with some granodioritic rocks. After the formations of OMG and OMTG, the emplacement of Singhbhum granites (SBGs) occurred in three phases, i.e., SBG I, SBG II, and SBG III [26]. SBG is the most widespread rock type in the SOC, occurring in an N-S elongated trend in the central part of the craton, covering an area of around 8000 Km^2 [26]. SBG hosts various rocks, such as biotite granodiorite, granite adamellitic, biotite trondhjemite, and leucogranite. At the boundary of the SBG, different rocks, such as chlorite epidote granodiorite and pyroxene diorite, have been found [26–28].

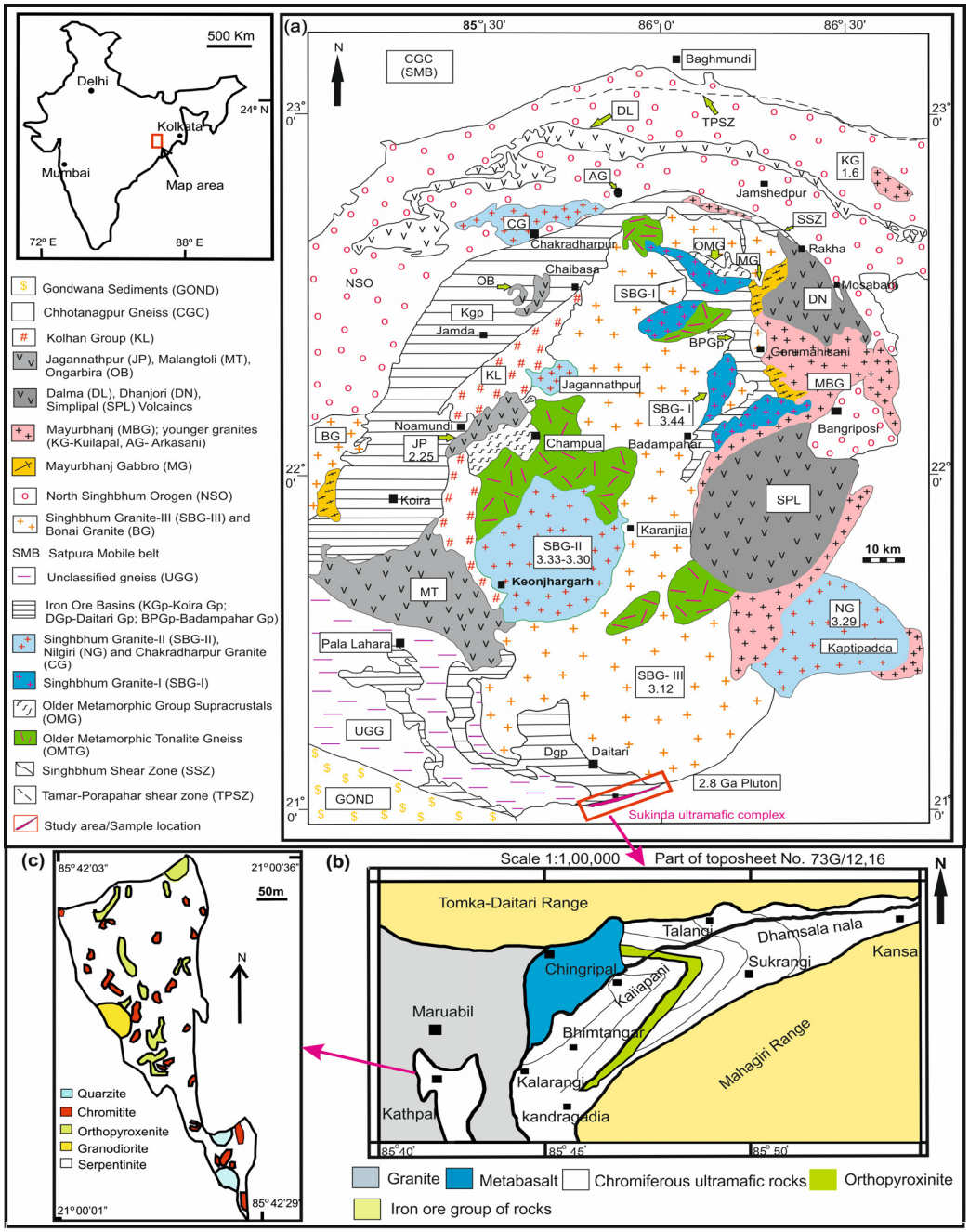

Figure 1. (**a**) Simplified geological map of Singhbhum Craton [10,13,26,28] and the location of the study area (box). (**b**) Geological map of Sukinda ultramafic complex [19,29]. (**c**) Geological map of Katpal area [29].

The Iron ore group (IOG) and Jagannathpur–Malangtoli–Simlipal–Dhanjori–Dalma lavas are volcanic–sedimentary formations bordering the Archean SBG batholith. The IOG supra-crustal successions consist of low-grade metamorphic sediments, including

meta-pelites, phyllites, tuffaceous shales, quartzites, and carbonates associated with mafic and felsic meta-volcanic and banded iron formations [26,30]. IOG formations also contain different forms of intrusive and extrusive igneous rocks, such as high-Mg rock varieties, komatiite, boninites, picrites, and siliceous high-Mg basalts [10,12,19,31–33]. The plutonic ultramafic suites are in a tabular form with economic chromite deposits and are associated with the Tomka–Daitari–Nuasahi–Sukinda belt [10]. The mafic intrusive bodies are found in the Nuasahi–Nilgiri–Gorumahisani–Badampahar areas [12]. Komatiites are present in the eastern IOG belt, such as Patharkata [34], Dhipasai (Tua Dungri hillock; [35]), and Kapili [36]. The subject of our current study, the Sukinda ultramafic complex, is located within the southeastern sector of the Tomka–Daitari basin, a component of the iron ore group formation [12,30]. Our study entailed a methodical collection of rock samples from two specific regions: Kaliapani (KLPN) and Katpal (KTPL).

There is a lack of geochronological data on the IOG and its age of formation; however, based on the intrusive field relationship, it is found that the period would have 3.2–3.1 Ga [23,37]. The U-Pb SHRIMP zircon age of dacite lava in the Tomka–Daitari basin is reported as 3.5 Ga [30]. The older rock formations of the SOC are intruded by newer mafic-ultramafic dyke (2600–950 Ma); this mafic–ultramafic intrusive is called 'newer dolerite dyke swarms' [24,38].

2.2. Local Geology

The Sukinda ultramafic complex is restricted within the eastern Ghats mobile belt and IOG and exposed along the southern margin of the Singbhum Craton. These ultramafic suites intrude along the marginal fracture of Singbhum crustal rocks in successive phases, and they are regional folds, forming a plunging synform. The plunging synform's northern limb shows a moderate dip, whereas the southern limb appears as sub-vertical [29,39]. The Sukinda ultramafic rocks consist of dunites, serpentinite, chromitite, and pyroxenite (Figure 1b). The exposed serpentinite in the Sukinda area is the low-grade metamorphic equivalent of dunites. Relatively fresh and unaltered pyroxenites are a late-stage intrusion into the early formed dunite and chromitite rock sequence. However, the regional disposition and relation with IOG suggest that the Sukinda ultramafic complex may be from the Precambrian age [22].

The rock samples were collected from the Kaliapni and Katpal areas of the Sukinda ultramafic complex for the present study. The Katpal area (Figure 1c) of the Sukinda ultramafic complex is situated in the southwestern part of the Kaliapani ultramafic unit (Figure 1b). In the Katpal area, dunite, serpentinites and chromitites are the major lithologic units. They are distributed randomly in fragments of different shapes within the coarse-grained gabbroic to granodioritic matrix, forming tectonic breccias [29]. The chromite grains of Katpal are dark black to dark brown. The Katpal chromites are texturally similar to Kaliapani chromites. The Katpal breccia of the gabbroic matrix consists of medium- to coarse-grained plagioclase, clinopyroxene, serpentine, amphibole, talc, quartz, and some chromites [29]. The studied ultramafic rocks were systematically sampled from different chromite host lithologies, specifically in the Kaliapani and Katpal chromite mines (Figure 2a,b). Field observations confirmed that dunites (Figure 2c) and serpentinized dunites were the predominant litho-unit in the area. Pyroxenites (Figure 2d) were associated with the serpentinized dunites as intrusive. Chromite ore bodies were interbedded within these two litho-units. The pyroxenite band contained fewer chromite minerals than the dunites. The fresh and unweathered samples (hand specimens), weighing several kilograms each, were collected from different mine sections.

Figure 2. (**a**,**b**) Field photographs of ultramafic rocks exposed in Sukinda chromite mines. (**c**,**d**) Ultramafic hand specimens collected from the Kaliapani area. (**e**,**f**) Ultramafic hand specimens collected from the Katpal area.

3. Samples and Analytical Methods

The samples of the Sukinda ultramafic complex were collected from the Kaliapani and Katpal areas, avoiding secondary veins (quartz and carbonates). The rock samples were powdered in a Retsch Vibratory Disc Mill RS 200 to a 300 mesh size in the Department of Applied Geology, IIT(ISM) Dhanbad. Major elements were determined by using pressed pellets in an X-ray fluorescence spectrometer (XRF; Rigaku ZSX Primus IV) at the Central Research Facility (CRF), IIT(ISM) Dhanbad, India. Pressed pellets (40 mm diameter) were prepared using collapsible aluminum cups. These cups were filled with boric acid, and about 2 g of the finely powdered sample was evenly sprayed and pressed under a hydraulic press at a 15-ton pressure to create a pellet (Hydraulic Press, Herzog, Germany). The rock standards used for the analysis were JH-1 and JGb-2. A duplicate analysis of the rock standard and certified values is given in Supplementary Table S1. The detection limits of the major and minor elements were ~0.001%, and the analytical precision and accuracy are given in Table S1. The major and minor oxides were recalculated on an anhydrous basis and presented in Table 1.

Table 1. Selected element (oxide) contents in weight percent (wt%) by XRF, or parts per million (ppm, $\mu g \cdot g^{-1}$) by HR-ICP-MS, in bulk whole-rock samples from Katpal. Kaliapani area of the Sukinda ultramafic complex. $Fe_2O_3{}^T$ represents total iron (oxide) content.

Species	Katpal					Kaliapani					
	1A	**3A**	**5A**	**2A**	**4A**	**8-11A**	**12-13A**	**X2A**	**21A**	**7A**	**X4A**
Main-element oxide contents in weight percent (wt%)											
SiO_2	42.14	42.31	44.76	46.44	54.31	37.83	40.06	40.26	47.5	50.21	53.79
TiO_2	0.12	0.1	0.06	0.02	0.1	0.02	0.01	0.01	0.02	0.02	0.03
Al_2O_3	3.23	3.08	1.86	1.1	3.11	1.13	0.74	0.79	1.22	0.92	1.16
$Fe_2O_3{}^T$	5.12	8.84	3.24	10.94	4.23	8.15	10.56	10.08	9.4	8.21	8.07
MnO	0.09	0.09	0.06	0.09	0.07	0.09	0.1	0.09	0.1	0.1	0.11
MgO	41.33	41.41	44.41	39.79	32.32	47.94	47.48	47.36	39.42	37.87	34.54
CaO	0.2	0.05	0.04	0.2	3.85	0.05	0.1	0.15	0.55	0.28	0.69
K_2O	n.d.	n.d.	n.d.	n.d.	n.d.	n.d.	n.d.	n.d.	0.01	n.d.	n.d.
Na_2O	0.16	0.15	0.15	0.15	0.15	0.17	0.17	0.16	0.18	0.16	0.18
P_2O_5	0.03	0.03	0.03	0.02	0.03	0.03	0.03	0.02	0.03	0.03	0.03
Cr_2O_3	7.29	3.01	4.27	1.05	1.05	4.59	0.75	0.8	1.16	1.08	1.1
NiO	0.13	0.09	0.7	0.04	n.d.	n.d.	n.d.	0.01	n.d.	0.91	n.d.
LOI	9.92	10.7	11.78	11.65	4.69	12.28	13.01	13.81	12.64	11.12	3.61
Analytical sum	109.76	109.85	111.37	111.47	103.91	112.29	113	113.55	112.22	110.9	103.3
Trace-element contents in parts per million (ppm, $\mu g \cdot g^{-1}$)											
Cr	58,799	28,159	26,785	7166	5492	18,778	3719	6370	5242	4140	905.4
Co	100.87	122.64	58.21	116.56	48.69	110.57	149.7	123.57	99.7	89.16	18.66
Ni	1660	1627	2311	1334	832	2225	2790	1947	1124	2759	193.81
Rb	1.93	1.4	7.75	0.98	1.23	27.31	45.94	10.92	8.71	27.27	3.58
Sr	11.98	4.22	204.83	3.74	7.05	188.04	257.42	227.53	127.73	227.41	20.44
Cs	0.13	0.1	0.17	0.08	0.13	0.84	1.4	0.25	0.09	0.45	0.06
Ba	11.84	20.06	65.28	9.77	7.13	60.19	87.67	64.07	42.36	92.12	16.33
Sc	9.91	9.31	7.4	8.69	15.68	7.09	8.5	4.77	7.14	7.38	2.31
V	150.57	104.95	94.55	49.87	85.34	104.25	73.54	41.88	32.94	39.33	10.05
Ta	0.02	0.02	0.01	0	0.07	0.02	0.01	0.01	0.01	0.01	0.02
Nb	0.15	0.14	0.14	0.08	0.53	0.12	0.1	0.07	0.04	0.07	0.57
Zr	7.07	5.9	2.99	1.75	4.85	6.16	5.65	0.96	0.6	1.27	2.23
Hf	0.16	0.14	0.07	0.04	0.12	0.15	0.13	0.02	0.01	0.03	0.04
Th	0.25	0.19	0.55	0.09	0.25	1.72	1.66	0.27	0.09	0.26	1.02
U	0.73	0.11	5.43	0.08	0.12	6.03	5.94	5.84	2.19	3.27	3.06
Y	3.36	1.46	4.77	0.77	5.1	9.48	10.84	2.43	0.89	6.14	1.96
Rrare-earth element (REE) contents in parts per million (ppm, $\mu g \cdot g^{-1}$)											
La	1.19	0.52	3.92	0.56	0.56	16.25	19.16	4.04	1.07	4.69	2.93
Ce	2.63	1.09	8.05	0.63	1.48	34.98	40.49	8.19	1.87	7.4	6.59
Pr	0.34	0.14	1.05	0.13	0.24	4.65	5.29	1.07	0.25	1.17	0.73
Nd	1.39	0.58	4.23	0.49	1.28	18.82	21.24	4.29	0.95	4.66	2.93
Sm	0.34	0.14	0.93	0.11	0.44	3.75	4.19	0.82	0.19	1.05	0.56
Eu	0.09	0.03	0.19	0.03	0.12	0.72	0.75	0.16	0.05	0.25	0.12
Gd	0.47	0.21	0.9	0.14	0.66	2.99	3.42	0.7	0.16	1.11	0.45
Tb	0.08	0.03	0.15	0.02	0.13	0.42	0.47	0.09	0.02	0.18	0.04
Dy	0.57	0.22	0.83	0.16	0.87	1.94	2.23	0.45	0.13	1	0.25
Ho	0.13	0.05	0.17	0.03	0.19	0.36	0.43	0.09	0.03	0.21	0.05
Er	0.39	0.16	0.5	0.1	0.55	0.93	1.07	0.24	0.08	0.57	0.13
Tm	0.06	0.03	0.08	0.02	0.08	0.12	0.14	0.04	0.01	0.08	0.01
Yb	0.4	0.2	0.44	0.12	0.5	0.66	0.75	0.18	0.08	0.45	0.15
Lu	0.06	0.03	0.07	0.02	0.07	0.09	0.11	0.03	0.02	0.07	0.01
Cu	15.37	8.29	46.31	5.96	6.11	120.61	144.75	54.06	32.87	62.57	120.67
Zn	80.2	71.85	396.68	48.24	42.82	355.11	755.22	221.36	337.46	574.29	759.94
Pb	22.16	11.03	24.16	8.3	5.73	32.54	38.86	16.01	13.99	23.94	9.96

Table 1. *Cont.*

Species	Katpal					Kaliapani					
	1A	**3A**	**5A**	**2A**	**4A**	**8-11A**	**12-13A**	**X2A**	**21A**	**7A**	**X4A**
	Calculated values and element (oxide) ratios										
Mg#	88.99	82.41	93.2	78.43	88.42	85.46	81.81	82.46	80.75	82.19	81.07
Al_2O_3/TiO_2	27.01	30.21	30.88	64.47	31.69	49.32	74.06	66	56.48	54.94	35.97
CaO/TiO_2	1.66	0.47	0.58	11.59	39.29	2.32	9.84	12.17	25.14	17	21.36
CaO/Al_2O_3	0.06	0.02	0.02	0.18	1.24	0.05	0.13	0.18	0.45	0.31	0.59
Ti/Sc	72.33	65.65	48.9	11.73	37.47	19.44	7.14	15.09	18.18	13.53	83.72
Ti/V	4.76	5.83	3.83	2.04	6.88	1.32	0.83	1.72	3.94	2.54	19.23
Ti/Zr	101.37	86.47	51.18	14.41	83.08	19.48	8.48	10.17	18.37	14.12	27.33
$(La/Yb)_{CN}$	3.12	0.93	5.5	2.08	2.5	7.08	3.11	15.49	17.46	16.7	1.13
$(La/Sm)_{CN}$	2.51	0.8	3.3	2.3	2.21	2.79	2.4	3.09	2.86	2.71	2.51
$(Gd/Yb)_{CN}$	0.96	0.84	1.64	0.95	1.07	3.66	3.71	3.2	1.69	1.98	2.43
$(Ce/Yb)_{CN}$	1.74	1.44	4.79	1.39	0.77	13.9	14.27	12.13	6.22	4.31	11.61
$(Tb/Yb)_{CN}$	0.93	0.75	1.47	0.87	1.11	2.81	2.84	2.36	1.33	1.82	1.26
$(Sm/Yb)_{CN}$	0.92	0.76	2.3	1.02	0.95	6.18	6.12	5.01	2.66	2.54	4.1
Ti/1000	0.72	0.61	0.36	0.1	0.59	0.14	0.06	0.07	0.13	0.1	0.19
Th/Ce	0.09	0.17	0.07	0.14	0.17	0.05	0.04	0.03	0.05	0.04	0.15
La/Yb	2.99	2.6	8.88	4.75	1.11	24.59	25.7	22.81	13.52	10.42	19.63
Dy/Yb	1.44	1.11	1.87	1.32	1.73	2.93	2.99	2.55	1.62	2.21	1.66
Nb/Zr	0.02	0.02	0.05	0.05	0.11	0.02	0.02	0.07	0.07	0.06	0.26
Th/Zr	0.04	0.03	0.19	0.05	0.05	0.28	0.29	0.28	0.15	0.21	0.46
Nb/Y	0.05	0.1	0.03	0.1	0.1	0.01	0.01	0.03	0.05	0.01	0.29
Rb/Y	0.57	0.96	1.62	1.26	0.24	2.88	4.24	4.5	9.83	4.44	1.83
Sc/Y	2.95	6.39	1.55	11.23	3.07	0.75	0.78	1.97	8.06	1.2	1.18
Zr/Hf	43.11	41.51	45.13	39.81	40.16	42.4	44.89	51.42	55.19	45.29	55.24
U/Th	2.98	0.59	9.84	0.93	0.48	3.5	3.59	21.65	23.92	12.41	3.01
Eu/Eu*	0.71	0.58	0.62	0.81	0.68	0.65	0.6	0.65	0.78	0.71	0.75
$(Th/Yb)_{PM}$	3.41	5.23	6.93	4.05	2.73	14.45	12.34	8.43	6.44	3.25	37.78
$(Th/Eu)_{PM}$	5.08	11.21	5.79	5.08	3.96	4.67	4.3	3.24	3.9	2.02	15.88
$(Eu/Yb)_{PM}$	0.67	0.47	1.2	0.8	0.69	3.1	2.87	2.6	1.65	1.61	2.38
$(Nb/Nb^*)_{PM}$	0.1	0.16	0.03	0.13	0.49	0.01	0.01	0.02	0.05	0.02	0.11
$(Ta/Ta^*)_{PM}$	0.22	0.35	0.04	0.12	1.17	0.02	0.01	0.07	0.11	0.03	0.06
$(Zr/Zr^*)_{PM}$	0.7	1.41	0.1	0.51	0.44	0.05	0.04	0.03	0.1	0.04	0.12
$(Hf/Hf^*)_{PM}$	0.6	1.26	0.08	0.47	0.4	0.04	0.03	0.03	0.06	0.03	0.08
$(Ti/Ti^*)_{PM}$	0.71	1.49	0.16	0.34	0.42	0.02	0.01	0.04	0.32	0.04	0.21

(n.d.) not detectable (below detection limit); ($_{CN}$) chondrite-normalized and ($_{PM}$) primitive-mantle-normalized distributions; normalization factors after [40]. Note that the analyses are reported on an anhydrous basis and LOI values are presented for informational purposes.

The trace and rare-earth element (REE) concentrations were determined by high-resolution inductively coupled plasma mass spectrometry (HR-ICP-MS; Nu Instruments Attom®, Wrexham, UK). The analysis was performed in jump–wiggle mode at a resolution of 300, allowing all the analytes of interest to be measured accurately. The instrument was optimized using a 1 ppb tuning solution, and the sensitivity of ^{114}In was about 1 million cps. The samples were prepared by using a closed-vessel digestion method. A total of 0.05 g of powdered samples were dissolved using an HF-HNO_3 acid mixture in a proportion of 7:3 in Savillexscrewtop vessels, and the acid mixture was kept on a hot plate at ~150 °C for 48 h. Following this, the vessels were opened and then we added one or two drops of $HClO_4$, which were evaporated at 150 °C for about 1 h to near-dryness. The remaining residues were dissolved by adding 10 mL of 1:1 HNO_3 and kept on a hot plate for 30–45 min at 80 °C to dissolve all the suspended particles. We transferred the prepared solution in a 250 mL standard flask, added 10 mL of 1:1 HNO_3 and 5 mL of Rh (Rhodium) solution as an internal standard, and the volume was made to reach 250 mL with Millipore water. Subsequently, the solution was finally stored in polyethylene bottles for the HR-ICP-MS analysis. A couple of procedural blanks were also prepared with the sample batch by

adopting the same protocol described above to negate any errors due to the reagent and handling issues. Certified reference materials UB-N (ANRT, France) and BHVO-1 (USGS) were dissolved simultaneously following the method described above and analyzed along with the samples. A duplicate analysis of the rock standard and certified values is given in Table S1, and the major element oxide in weight percentage (wt%) and trace-element and REE contents are presented in Table 1. The detailed analytical technique, instrument setting, analytical condition, and lower detection limit refer to [41].

The mineral chemistry of the silicate minerals and chromite grains was analyzed by CAMECA SX five electron probe micro-analysis (EPMA) at the Central Research Facility (CRF), IIT(ISM) Dhanbad, Jharkhand. This instrument was equipped with four wavelength-dispersive spectrometers (WDSs). Before the EPMA analysis, the polish sections were coated with ~20 nm of carbon in a Cressington 108 carbon/A coater to minimize the electron beam's charging rate. The analysis was performed at a high-vacuum setting (10^{-6} Torr), with a 1–3 µm electron beam diameter at the point of incidence, operated at an accelerating voltage of 15 KeV, and the beam used a 20 nA probe current as measured using the Faraday cup. Spectra were collected for 30 s at the peak and 10 s in the background. The internal mineral standards used for the calibration were periclase (Mg), orthoclase (K, Al), apatite (Ca, P), hematite (Fe), albite (Si, Na), synthetic rutile TiO_2 (Ti), synthetic eskolaite Cr_2O_3 (Cr), rhodonite (Mn), and Ni (NiO). Raw data were corrected using proprietary CAMECA software applying a ZAF algorithm. The structural calculation of the analyzed minerals was performed by a stoichiometry process. The amounts of Fe^{3+} and Fe^{2+} in the chromites were calculated according to the charge balance equation [42]. Net lower limits of detection (LLDs) for the relevant concentration intervals were listed per oxide species in a separate column in the data, as per [43]. The selected mineral chemistry data are presented in Tables 2–5.

Table 2. Selected main-element oxide contents in weight percent (wt%) by EPMA in olivine from the Sukinda ultramafic complex. Calculated Fe_2O_3 and FeO (cf. guidelines from Droop (1987)) [42]. Oxide contents recast into numbers of cations in atoms per formula unit (cf. Deer et al. (2013)) [44]. Further explanation in the text. (n.d.) not detectable (below detection limit).

	LLD%	X7-1	X7-5	X6-10	X6-13	X2-11	X2-9	X5U-13	X9-3	X5U-15	X2-7	X9-10
Main-element oxide contents in weight percent (wt%)												
SiO_2	<0.07	40.93	41.42	41.30	41.07	41.88	41.54	40.89	41.17	41.01	41.87	40.89
Al_2O_3	<0.05	n.d.	n.d.	n.d.	n.d.	n.d.	n.d.	0.05	0.05	n.d.	n.d.	n.d.
Fe_2O_3		0.84	0.63	0.92	0.97	0.97	0.96	0.93	0.88	0.84	0.99	0.94
FeO	<0.22	6.80	5.11	7.46	7.87	7.83	7.81	7.52	7.14	6.79	8.00	7.60
MgO	<0.06	49.70	51.40	49.86	49.57	49.97	49.61	49.16	49.40	49.98	50.26	48.96
MnO	<0.24	n.d.	n.d.	n.d.	n.d.	0.24	n.d.	n.d.	0.31	n.d.	n.d.	n.d.
NiO	<0.04	0.40	0.44	0.19	0.24	0.11	0.25	0.23	0.49	0.40	0.13	0.23
CaO	<0.05	0.09	0.07	0.15	0.11	0.09	0.03	0.17	0.11	0.12	0.03	0.10
Analytical sum		98.76	99.07	99.88	99.83	101.09	100.21	98.95	99.55	99.13	101.28	98.71
Numbers of cations in atoms per formula unit (apfu) on the basis of 4O												
Mg		1.817	1.858	1.808	1.802	1.792	1.792	1.801	1.799	1.821	1.797	1.797
Fe^{2+}		0.14	0.104	0.152	0.16	0.157	0.158	0.155	0.146	0.139	0.161	0.156
Ca		0.002	0.002	0.004	0.003	0.002	0.001	0.004	0.003	0.003	0.001	0.002
Mn		n.d.	n.d.	n.d.	n.d.	0.005	n.d.	n.d.	0.006	n.d.	n.d.	n.d.
Ni		0.008	0.009	0.004	0.005	0.002	0.005	0.005	0.01	0.008	0.003	0.005
Al		n.d.	n.d.	n.d.	n.d.	n.d.	n.d.	0.001	0.001	n.d.	n.d.	n.d.
Fe^{3+}		0.015	0.012	0.017	0.018	0.017	0.018	0.017	0.016	0.015	0.018	0.017
Σ		1.982	1.985	1.985	1.988	1.975	1.974	1.983	1.981	1.986	1.98	1.977
Si		1.004	1.004	1.005	1.002	1.007	1.007	1.005	1.006	1.002	1.004	1.007
Σ		1.004	1.004	1.005	1.002	1.007	1.007	1.005	1.006	1.002	1.004	1.007
Calculated values												
Mg#		0.929	0.947	0.923	0.918	0.919	0.919	0.921	0.925	0.929	0.918	0.92
Forsterite		92.14	94.16	91.47	91	91.1	91.06	91.29	91.74	92.2	90.97	91.18

Table 3. Selected main-element oxide contents in weight percent (wt%) by EPMA in orthopyroxene from Sukinda ultramafic complex. Fe_2O_3 and FeO calculated (cf. guidelines from Droop (1987)). Oxide contents recast into numbers of cations in atoms per formula unit (cf. Deer et al. (2013)). Further explanation in text. (n.d.) not detectable (below detection limit).

	LLD%	X1-16	X2-20	X3-27	X4-16	X5-26	A-17	B-22	C-31	D-39
Main-element oxide contents in weight percent (wt%)										
SiO_2	<0.07	57.72	58.07	57.56	57.72	57.59	58.41	57.88	58.18	58.19
TiO_2	<0.05	n.d.	n.d.	n.d.	n.d.	n.d.	n.d.	n.d.	n.d.	0.06
Al_2O_3	<0.05	0.71	0.75	0.8	0.71	0.68	0.7	0.69	0.73	0.72
Cr_2O_3	<0.04	0.64	0.67	0.51	0.64	0.58	0.56	0.54	0.59	0.56
Fe_2O_3		n.d.	n.d.	0.461	0.767	n.d.	n.d.	n.d.	n.d.	n.d.
FeO	<0.22	5.52	5.56	5.425	4.831	5.68	5.43	5.41	5.31	5.46
MgO	<0.06	34.52	34.34	34.82	34.52	34.48	34.12	34.41	34.1	34.49
MnO	<0.24	0.3	n.d.	n.d.	0.3	n.d.	n.d.	n.d.	n.d.	n.d.
NiO	<0.04	n.d.	n.d.	0.18	n.d.	0.09	n.d.	n.d.	n.d.	n.d.
Na_2O	<0.06	n.d.	n.d.	n.d.	n.d.	0.06	n.d.	n.d.	n.d.	n.d.
CaO	<0.05	0.6	0.68	0.65	0.6	0.62	0.75	0.76	0.76	0.69
Analytical sum		100.01	100.07	100.41	100.09	99.78	99.97	99.69	99.67	100.17
Numbers of cations in atoms per formula unit (apfu) on the basis of 6O										
Si	-	1.985	1.991	1.972	1.989	1.984	2.003	1.99	1.999	1.993
Al^{IV}	-	0.015	0.009	0.028	0.011	0.016	0	0.01	0.001	0.029
Σ		2	2	2	2	2	2.003	2	2	2
Al^{VI}	-	0.014	0.021	0.004	0.018	0.012	0.028	0.018	0.029	0.022
Cr	-	0.017	0.018	0.014	0.017	0.016	0.015	0.015	0.016	0.015
Ni	-	n.d.	n.d.	0.005	n.d.	0.002	n.d.	n.d.	n.d.	n.d.
Fe^{3+}	-	n.d.	n.d.	0.012	0.02	n.d.	n.d.	n.d.	n.d.	n.d.
Ti	-	n.d.	n.d.	n.d.	n.d.	n.d.	n.d.	n.d.	n.d.	0.002
Mg	-	1.769	1.755	1.778	1.773	1.771	1.744	1.764	1.746	1.761
Fe^{2+}	-	0.159	0.159	0.155	0.139	0.164	0.156	0.156	0.153	0.156
Mn	-	0.009	n.d.	n.d.	0.009	n.d.	n.d.	n.d.	n.d.	n.d.
Ca	-	0.022	0.025	0.024	0.021	0.023	0.028	0.028	0.028	0.025
Na	-	n.d.	n.d.	n.d.	n.d.	0.004	n.d.	n.d.	n.d.	n.d.
Σ		1.99	1.978	1.992	1.997	1.992	1.971	1.981	1.972	1.981
Calculated values										
Mg#	-	0.918	0.917	0.92	0.927	0.915	0.918	0.919	0.92	0.918
Cr#	-	0.377	0.375	0.3	0.377	0.364	0.349	0.344	0.352	0.343

Table 4. Selected main-element oxide contents in weight percent (wt%) by EPMA in chromite from the Kaliapani area. Calculated Fe_2O_3 and FeO (cf. guidelines from Droop (1987)). Oxides content recast into numbers of cations in atoms per formula unit (cf. Deer et al. (2013)). Further explanation in text. (n.d.) not detectable (below detection limit).

	LLD%	X6-17	X2-4	X2-5	X8-9	X8-13	X8-27	X2-2	X2-4	X2-4/1	X2-6/1	X9-8	X9-9
Main-element oxide contents in weight percent (wt%)													
SiO_2	<0.07	n.d.	n.d.	n.d.	n.d.	n.d.	n.d.	n.d.	n.d.	n.d.	n.d.	0.08	0.1
TiO_2	<0.05	0.17	0.17	0.14	0.19	0.18	0.15	0.20	0.18	0.17	0.19	0.18	0.17
Al_2O_3	<0.05	8.92	15.30	15.12	12.13	12.04	12.36	13.15	13.57	15.14	13.68	14.50	14.51
Cr_2O_3	<0.04	60.45	55.33	55.15	57.50	57.92	58.63	55.57	55.44	55.22	54.24	55.17	54.90
Fe_2O_3		2.84	0.25	0.95	1.90	1.22	0.31	2.24	1.93	0.88	3.38	1.19	0.86
FeO	<0.22	18.06	17.09	17.43	19.19	20.06	20.46	20.60	19.52	17.33	19.45	16.90	17.87
MgO	<0.06	9.90	11.15	10.72	9.72	9.00	8.83	8.92	9.65	11.16	9.79	11.33	10.62
MnO	<0.24	0.42	n.d.	0.30	0.35	0.47	0.39	0.37	0.29	0.34	n.d.	0.25	0.26
NiO	<0.04	0.16	0.07	n.d.	n.d.	0.10	0.25	n.d.	n.d.	n.d.	0.08	n.d.	n.d.
CaO	<0.05	n.d.	n.d.	0.05	n.d.	n.d.	n.d.	n.d.	n.d.	n.d.	n.d.	n.d.	n.d.

Table 4. *Cont.*

	LLD%	X6-17	X2-4	X2-5	X8-9	X8-13	X8-27	X2-2	X2-4	X2-4/1	X2-6/1	X9-8	X9-9
Analytical sum		100.92	99.37	99.86	100.98	100.98	101.37	101.05	100.58	100.24	100.81	99.52	99.19
Numbers of cations in atoms per formula unit (apfu) on the basis of 4O													
Si	-	n.d.	n.d.	n.d.	n.d.	n.d.	n.d.	n.d.	n.d.	n.d.	n.d.	0.003	0.003
Al	-	0.347	0.58	0.573	0.465	0.464	0.475	0.505	0.519	0.571	0.521	0.551	0.555
Cr	-	1.575	1.407	1.403	1.479	1.498	1.51	1.43	1.423	1.396	1.386	1.406	1.409
Fe^{3+}	-	0.07	0.006	0.023	0.047	0.03	0.008	0.055	0.047	0.021	0.082	0.029	0.021
Ti	-	0.004	0.004	0.003	0.005	0.004	0.004	0.005	0.004	0.004	0.005	0.004	0.004
Σ		1.996	1.997	2.002	1.996	1.996	1.997	1.995	1.993	1.992	1.994	1.993	1.992
Mg	-	0.487	0.535	0.514	0.471	0.439	0.429	0.433	0.467	0.532	0.472	0.545	0.514
Fe^{2+}	-	0.498	0.46	0.469	0.522	0.549	0.557	0.561	0.53	0.464	0.526	0.456	0.485
Ni	-	0.004	0.002	n.d.	n.d.	0.003	0.007	n.d.	n.d.	n.d.	0.002	n.d.	n.d.
Mn	-	0.012	n.d.	0.008	0.01	0.013	0.011	0.01	0.008	0.009	n.d.	0.007	0.007
Ca	-	n.d.	n.d.	0.002	n.d.	n.d.	n.d.	n.d.	n.d.	n.d.	n.d.	n.d.	n.d.
Σ		1.001	0.997	0.993	1.003	1.004	1.004	1.004	1.005	1.005	1	1.008	1.006
Calculated values													
Mg#	-	0.494	0.538	0.523	0.474	0.444	0.435	0.436	0.468	0.534	0.473	0.544	0.514
Cr#	-	0.82	0.708	0.71	0.761	0.763	0.761	0.739	0.733	0.71	0.727	0.719	0.717
Fe^{3+} ratio	-	0.035	0.003	0.011	0.023	0.015	0.004	0.028	0.024	0.011	0.041	0.015	0.011
$(Al_2O_3)_{melt}$	-	9.93	12.82	12.76	11.58	11.54	11.68	12.01	12.18	12.76	12.22	12.53	12.54
$(TiO_2)_{melt}$	-	0.27	0.27	0.23	0.30	0.29	0.25	0.31	0.29	0.27	0.30	0.29	0.27

Table 5. Selected main-element oxide contents in weight percent (wt%) by EPMA in chromite from the Katpal area. Calculated Fe_2O_3 and FeO (cf. guidelines from Droop (1987)). Oxide contents recast into numbers of cations in atoms per formula unit (cf. Deer et al. (2013)). Further explanation in the text. (n.d.) not detectable (below detection limit).

	LLD%	2A	9	13	14	22	23	26	33	36	39	40	41	43
SiO_2	<0.07	n.d.	n.d.	0.09	0.07	0.1	n.d.	n.d.	n.d.	0.07	n.d.	0.09	n.d.	n.d.
TiO_2	<0.05	0.25	0.21	0.29	0.19	0.27	0.30	0.27	0.21	0.20	0.16	0.24	0.21	0.24
Al_2O_3	<0.05	12.98	13.63	12.74	15.42	14.42	15.25	13.06	13.05	12.01	11.59	11.32	12.51	11.92
Cr_2O_3	<0.04	53.07	52.56	54.05	50.27	51.50	50.17	52.91	53.70	55.64	56.76	56.14	54.72	56.05
Fe_2O_3		3.44	3.21	3.43	4.09	3.38	4.23	3.98	3.61	3.39	3.48	3.92	4.22	3.84
FeO	<0.22	21.40	21.17	21.66	21.26	21.31	21.44	21.12	18.23	18.22	17.94	17.52	18.18	18.12
MgO	<0.06	8.19	8.40	8.18	8.40	8.21	8.44	8.24	10.09	10.21	9.78	10.24	10.36	9.88
MnO	<0.24	0.41	0.29	0.51	0.58	0.56	0.38	0.44	0.36	0.30	0.47	0.24	0.40	0.29
NiO	<0.04	n.d.	n.d.	n.d.	n.d.	n.d.	n.d.	0.12	n.d.	n.d.	0.09	0.09	n.d.	0.10
Na_2O	<0.06	n.d.	n.d.	n.d.	n.d.	n.d.	n.d.	n.d.	n.d.	n.d.	0.09	0.09	n.d.	0.10
CaO	<0.05	n.d.	n.d.	n.d.	n.d.	n.d.	n.d.	n.d.	n.d.	n.d.	n.d.	n.d.	n.d.	n.d.
Analytical sum		99.74	99.47	100.86	100.22	99.64	100.21	100.13	99.25	99.97	100.36	99.80	100.60	100.54
Numbers of cations in atoms per formula unit (apfu) on the basis of 4O														
Si		n.d.	n.d.	0.003	0.002	0.003	n.d.	n.d.	n.d.	0.002	n.d.	0.003	n.d.	n.d.
Al		0.507	0.531	0.493	0.592	0.559	0.587	0.508	0.505	0.463	0.447	0.438	0.479	0.459
Cr		1.39	1.374	1.403	1.295	1.34	1.294	1.381	1.395	1.44	1.47	1.458	1.405	1.447
Fe^{3+}		0.086	0.08	0.085	0.1	0.084	0.104	0.099	0.089	0.084	0.086	0.097	0.103	0.094
Ti		0.006	0.005	0.007	0.005	0.007	0.007	0.007	0.005	0.005	0.004	0.006	0.005	0.006
Σ		1.989	1.99	1.991	1.994	1.993	1.992	1.995	1.994	1.994	2.007	2.002	1.992	2.006
Mg		0.405	0.414	0.4	0.408	0.403	0.411	0.405	0.494	0.498	0.478	0.502	0.502	0.481
Fe^{2+}		0.593	0.585	0.595	0.58	0.587	0.585	0.583	0.501	0.499	0.491	0.481	0.494	0.495
Ni		n.d.	n.d.	n.d.	n.d.	n.d.	n.d.	0.003	n.d.	n.d.	0.002	0.002	n.d.	0.003
Mn		0.012	0.008	0.014	0.016	0.016	0.011	0.012	0.01	0.008	0.013	0.007	0.011	0.008
Ca		0	0	0	0	0	0	0	0	0	0	0	0	0
Na		n.d.	n.d.	n.d.	n.d.	n.d.	n.d.	n.d.	n.d.	n.d.	0.006	0.006	n.d.	0.006

Table 5. *Cont.*

LLD%	2A	9	13	14	22	23	26	33	36	39	40	41	43
Σ	1.01	1.007	1.009	1.004	1.006	1.007	1.003	1.005	1.005	0.99	0.998	1.007	0.993
Calculated values													
Mg#	0.405	0.414	0.402	0.413	0.407	0.412	0.410	0.497	0.500	0.493	0.510	0.504	0.493
Cr#	0.733	0.721	0.740	0.686	0.706	0.688	0.731	0.734	0.757	0.767	0.769	0.746	0.759
Fe^{+3}-ratio	0.043	0.040	0.043	0.050	0.042	0.052	0.050	0.045	0.042	0.043	0.049	0.052	0.047
$(Al_2O_3)_{melt}$	11.94	12.20	11.84	12.86	12.50	12.80	11.97	11.97	11.52	11.33	11.21	11.74	11.48
$(TiO_2)_{melt}$	0.38	0.33	0.43	0.30	0.40	0.44	0.40	0.33	0.31	0.26	0.36	0.33	0.36

4. Results

4.1. Petrography

The studied ultramafic rocks were systematically sampled from different chromite host lithologies, specifically in the Kaliapani and Katpal chromite mines (Figure 2a,b). Field observations confirmed that the dunites and serpentinized dunites were the predominant litho-unit in the area. Pyroxenites were associated with the dunite and serpentinized dunite as intrusive. The chromite ore bodies were interbedded within these two litho-units. The pyroxenite band contained less chromite minerals than the dunites. The fresh and unweathered samples (hand specimens), weighing several kilograms each, were collected from different mine sections. Thin sections were analyzed for a petrographic study and prepared using Struers and Buehler equipment [45]. Epoxy additives were used in to create the thin sections. The 30 µm thin sections were polished using diamond pastes at 6–4–3–0.25 µm on cloth. In incident- and transmitted-illumination settings, the polished sections were studied using an optical Nikon Eclipse E200 petrographic microscope.

4.1.1. Dunite

The fresh and unaltered dunite samples were collected from the mine sections for petrographic and geochemical studies. The dunites appeared as dusty green in the hand specimen (Figure 2c,e). The primary mineral phases of the dunite are olivines, which are rarely altered to serpentine in some places but retain the protolith's primary cumulate structure. The mineral grains in the dunite were medium to coarse in size and subhedral to euhedral in shape (Figure 3b). The large euhedral to subhedral grains of olivine were highly deformed and fractured (Figure 3b). The dunite host disseminated chromite grains as an accessory mineral phase. The chromite grains were fine to medium in size and euhedral in shape, which could be observed under the microscope. Chromite grains were observed along with cumulus olivines. The rounded shape of poikilitically included chromite grains within the olivine was primarily attributed to the process of resorption. They appeared as either opaque or a dark reddish-brown color (Figure 3b).

4.1.2. Orthopyroxenite

In the hand specimen, the orthopyroxenite appeared dark greenish and coarse-grained (Figure 2d). The orthopyroxenites were relatively less altered. Under the microscope, the orthopyroxenites were medium to coarse grained and showed euhedral to subhedral orthopyroxene grains with a granoblastic texture. The orthopyroxenite primarily comprised the enstatite orthopyroxene mineral phases (Figure 3a,c). In the photomicrograph, the pyroxenes showed exosolution lamellae. These lamellae resulted from the exsolution of a separate pyroxene phase due to sub-solidus re-equilibrium occurring during successive slow cooling. Accessory chromite mineral phases were rarely observed in the orthopyroxenite compared to dunite.

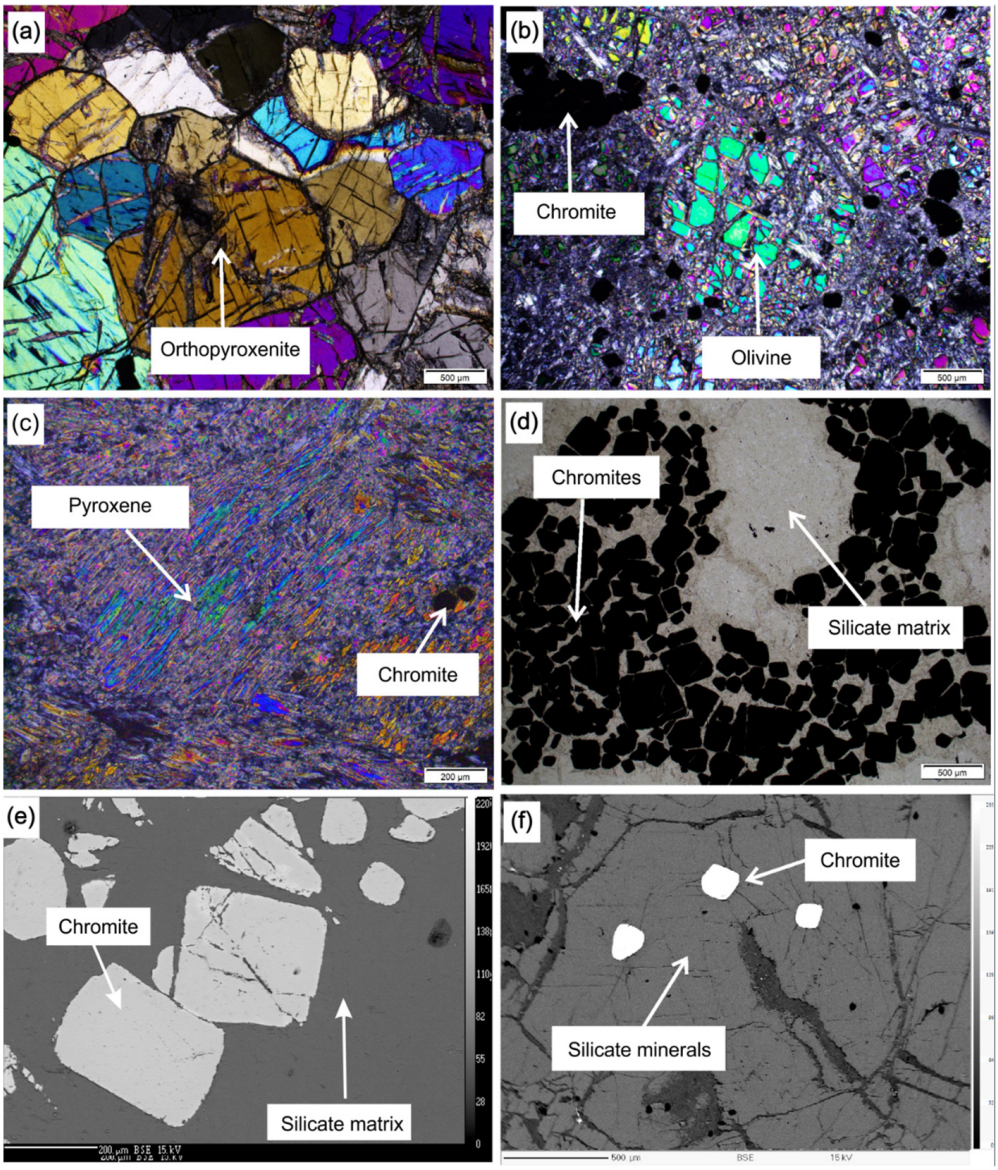

Figure 3. (**a**) Orthopyroxenite (enstatite mineral grains with much fewer chromite grains). (**b**) Dunite (olivine grain surrounded by chromite grains and the serpentine minerals developed in the fractures). (**c**) Pyroxene (larger grains of pyroxene with small patches of chromite). (**d**) Traces of weathered silicate mineral grains surrounded by chromite grains. (**e**) BSE image of chromite grains surrounded by silicate matrix. (**f**) BSE image of orthopyroxenite, gray minerals are enstatite, and the light-colored mineral grains are chromite.

4.1.3. Serpentinite

The original cumulate textures from previous stages were still evident in the serpentinite (Figure 2f), where remnants of olivine could be observed dispersed throughout the matrix. The serpentinization process occurred more extensively along the fractures and fissures (Figure 3b). As serpentinization progressed, it gradually removed the bulk of olivine and orthopyroxene, leaving only their skeletal structures behind. In the later stages, these skeletal structures were no longer present in the final mineral compositions of the serpentinite (Figure 3d). However, the serpentinite litho-types were not considered for the geochemical analysis and interpretation.

The observed textures in the Sukinda area's ultramafic rocks provide valuable insights into the sequence of crystallization events. These rocks exhibit a distinct pattern of mineral formation, starting with olivine, followed by a combination of olivine and chromite, then

a mix of olivine and orthopyroxene, and, finally, orthopyroxene. As olivine continues to crystallize, the composition of the magma gradually shifts towards the olivine–chromite cotectic point, leading to the simultaneous precipitation of both olivine and chromite phases. In the Sukinda region, once chromitite formation and the primary ultramafic mass crystallization occurred within the upper mantle conditions, the remaining magma underwent a further evolution, reaching a composition dominated by orthopyroxene.

4.2. Whole-Rock Geochemistry

4.2.1. Major-Element Geochemistry

The Sukinda ultramafics of the KTPL area showed high Mg# (78.43 to 93.20 wt%) and low to moderate $Fe_2O_3{}^t$ (3.24 to 10.94 wt%), CaO (0.04 to 3.85 wt%), SiO_2 (42.14 to 54.31 wt%), TiO_2 (0.02 to 0.12 wt%), Al_2O_3(1.10 to 3.23 wt%), and Na_2O contents (0.15 to 0.16 wt%), whereas the Cr_2O_3 concentration varied from 1.05 to 7.29 wt% and NiO from 0.04 to 0.70 wt%.

The KLPN area showed high Mg# (80.75 to 85.46 wt%) and low $Fe_2O_3{}^t$ (8.07 to 10.56 wt%), CaO (0.05 to 0.69 wt%), SiO_2 (37.83 to 53.79 wt%), TiO_2 (0.01 to 0.03 wt%), Al_2O_3 (0.74 to 1.22 wt%), and Na_2O contents (0.16 to 0.18 wt%), whereas the Cr_2O_3 concentration varied from 0.75 to 4.59 wt%. and the NiO concentration ranged between 0.01 and 0.91 wt%.

While the KTPL samples exhibited a broad spectra of Cr_2O_3, Fe_2O_3, and CaO contents, the KLPN samples demonstrated a more restricted range of these oxides. The KTPL samples exhibited elevated Ti values, primarily attributed to the presence of Ti-V-bearing iron oxide minerals, while the KLPN samples presented higher Fe values due to the presence of magnetite iron oxide as an accessory phase.

The samples from the Sukinda ultramafic complex showed distinct major and minor oxide distributions. The bi-variant diagrams of MgO versus other major and minor elements were plotted for Sukinda ultramafic rocks (Figure 4). The Sukinda ultramafic samples displayed a negative trend between MgO vs. SiO_2, a scattered pattern between MgO and $Fe_2O_3{}^t$, and a negative trend between MgO vs. TiO_2 (Figure 4). The negative correlation between MgO versus SiO_2, TiO_2, and Al_2O_3 suggested the fractional crystallization of the parental magma from which the Sukinda ultramafic rocks were formed. The positive correlation of MgO versus Cr (ppm) and Ni (ppm) was due to the fractionation of early cumulus olivine and chromite crystals from the parental magma.

4.2.2. Trace-Element Geochemistry

The ultramafics of the Katpal samples showed different compatible trace-element concentrations for Cr (5492 to 58,799 ppm), Ni (831.75 to 2311 ppm), and V (49.87 to 150.57 ppm), and the incompatible elements showed variations in Zr (1.75 to7.07 ppm), Sr (3.74 to 204.83 ppm), Cs (0.08 to 0.17 ppm), U (0.08 to 5.43 ppm), Th (0.09 to 0.55 ppm), Y (0.77 to 5.10 ppm), Nb (0.08 to 0.53 ppm), and Rb (0.98 to 7.75 ppm).

The total REE value of the Katpal ultramafics showed a narrow range of variation from 2.56 to 21.50 ppm, with there was limited REE fractionation. The $(Ce/Yb)_{CN}$ ratios varied from 0.77 to 4.79, LREE values varied from $(La/Sm)_{CN}$ = 0.79 to 3.17, MREE values varied from $(Sm/Yb)_{CN}$ = 0.76 to 2.30, and presented a limited fractionation of HREE $(Gd/Yb)_{CN}$ = 0.84 to 1.64 with a negative Eu anomaly (Eu/Eu* = 0.58 to 0.81). The chondrite-normalized REE distribution diagram (Figure 5a) of the Katpal ultramafics was characterized by a weak enrichment of LREE, flat HREE, and negative Eu anomalies (Eu/Eu* = 0.58 to 0.81).

In the primitive mantle-normalized trace-element plots (normalization values were obtained from McDonough et al. (1995) [40] (Figure 5b), the incompatible elements of Katpal rocks displayed a negative correlation $([Th/Yb]_{PM}$ = 2.73 to 6.93) $([Th/Eu]_{PM}$ = 3.96 to 11.21), and the compatible elements displayed a relatively positive to flat pattern $([Eu/Yb]_{PM}$ = 0.47 to 1.20). The primitive mantle-normalized trace-element plot displayed significant negative anomalies for several elements, including Nb ([Nb/Nb*] = 0.03 to 0.49), Ta ([Ta/Ta*] = 0.04 to 0.35, except for one sample that showed 1.17), Zr ([Zr/Zr*] = 0.10

to 0.70, except for one sample, KTPL-3A, which showed 1.41), Hf ([Hf/Hf*] = 0.08 to 0.60, except for one sample, KTPL-3A, which showed 1.26), and Ti ([Ti/Ti*] = 0.16 to 0.71, except for one sample, KTPL-3A, which showed 1.49). These negative anomalies indicated depletions in these elements relative to the primitive mantle.

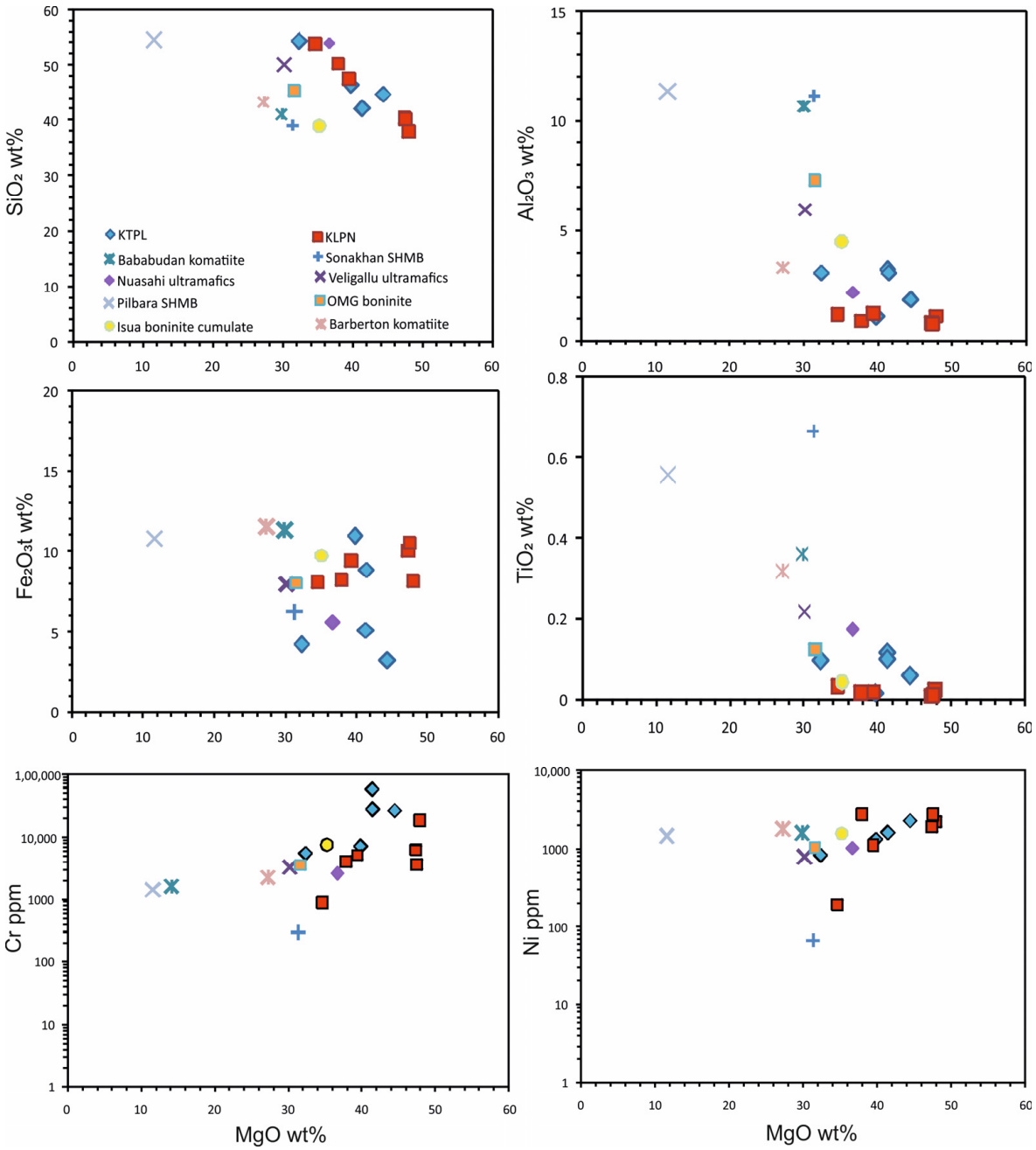

Figure 4. Variation diagram of MgO versus Al_2O_3, SiO_2, Cr, Ni, TiO_2, O, and $Fe_2O_3{}^t$ in Sukinda ultramafic complex and different high-Mg rocks (i.e., boninites, siliceous high-Mg basalts, and komatiites) in the world. The data are obtained after OMG boninite [46], Nuasahi boninite [9], Bababudan komatiite [47], Veligallu ultramafic [48], Sonakhan SHMB [49], Barberton komatiite [50], Pilbara SHMB [51], and Isua boninite cumulate [52].

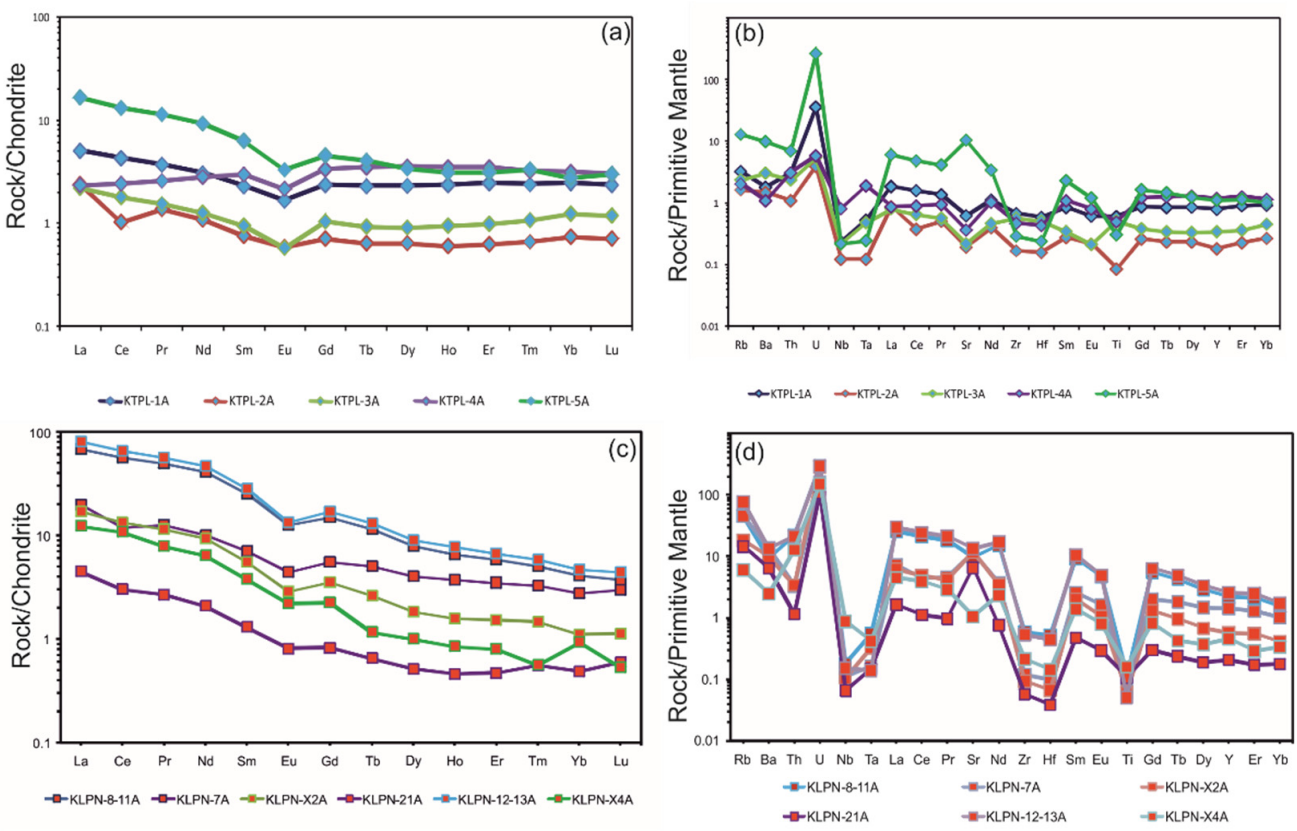

Figure 5. Chondrite-normalized rare-earth element patterns and primitive mantle-normalized multi-element plots of Sukinda ultramafic rocks. (**a**,**b**) Plotted for Kaliapani and (**c**,**d**) Katpal samples. For normalization, chondrite and primitive mantle values are taken from McDonough et al. (1995) [45].

The total REE value of Kaliapani ultramafics varied from 4.89 to 99.72 ppm, with limited REE fractionation $(Ce/Yb)_{CN}$ ratios varying from 4.31 to 14.27, LREE values varying from $(La/Sm)_{CN}$ = 2.70 to 3.45), MREE values varying from $(Sm/Yb)_{CN}$ = 2.54 to 6.18, and HREE values varying from $(Gd/Yb)_{CN}$ = 1.69 to 3.71) with a negative Eu anomaly (Eu/Eu* = 0.60 to 0.78). The chondrite-normalized diagram (Figure 5c) of the Kaliapani ultramafics shows a negative-sloping REE pattern with LREE enrichment and a slightly negative Eu anomaly (Eu/Eu* = 0.60 to 0.78).

Relative to the Katpal samples, the Kaliapani samples were characterized by a high REE concentration and LREE enrichment. Relative to the Katpal samples, the trace elements in the Kaliapani samples were characterized by low concentrations of Zr (0.60 to 6.16 ppm); Cr (905.40 to 18,778 ppm); Ni (193.81 to 2790 ppm); and V (10.05 to 104.25 ppm), and high concentration of Sr (20.44 to 257.42 ppm), Cs (0.06 to 1.40 ppm), U (2.19 to 6.03 ppm), Th (0.09 to 1.72 ppm), Y (0.89 to 10.84 ppm), Nb (0.04 to 0.57 ppm), and Rb (3.58 to 45.94 ppm).

The primitive mantle-normalized trace-element plots (Figure 5d) of the Kaliapani rocks displayed a negative sloping pattern ($[Th/Yb]_{PM}$ = 3.25 to 37.78), the incompatible elements had negative slopes ($[Th/Eu]_{PM}$ = 2.02 to 15.88), and the compatible elements displayed a relatively flat to negative pattern ($[Eu/Yb]_{PM}$ = 1.61 to 3.1). The primitive mantle-normalized trace-element plot showed prominent negative anomalies of Nb = ([Nb/Nb*] = 0.01 to 0.11), Ta = ([Ta/Ta*] = 0.01 to 0.11), Zr = ([Zr/Zr*] = 0.03 to 0.12), Hf = ([Hf/Hf*] = 0.03 to 0.08), and Ti = ([Ti/Ti*] = 0.01 to 0.32).

The Kathpal ultramafics displayed a limited range of variation in their total REE values, ranging from 2.56 to 21.50 ppm, with minimal REE fractionation. On the other hand, the Kaliapani ultramafics exhibited a broader spectrum in total REE values, spanning from 4.89 to 99.72 ppm, signifying significant variability. In contrast to the Kathpal samples, the Kaliapani samples were characterized by elevated REE concentrations and a preferential

enrichment of LREE. The Kathpal ultramafics demonstrated a mild LREE enrichment, a relatively uniform distribution of HREE, and negative Eu anomalies (Eu/Eu* = 0.58 to 0.81). In comparison, the Kaliapani ultramafics presented a descending REE pattern with LREE enrichment and a slightly negative Eu anomaly (Eu/Eu* = 0.60 to 0.78). The high trace-element concentration, higher range in total REE values, and elevated LREE concentration of the KLPN samples relative to KTPL samples suggested that the KLPN samples may have interacted with more evolved melt during the secondary melting phase or the fractionation process.

4.3. Mineral Chemistry

4.3.1. Chromite

Chromite grain occurred as an independent phase in the Sukinda ultramafic rocks. The analyses of chromites from dunites were taken into consideration in this study. The Cr numbers, Cr# = [Cr/(Cr + Al), molar ratio], of chromites in the dunite in the Kaliapani and Katpal areas varied from 0.70 to 0.82 and 0.68 to 0.76; the Mg number, Mg# = [Mg/(Mg + Fe^{2+}) molar ratio], of chromites in the dunite varied from 0.43 to 0.54 and 0.40 to 0.51; and the iron number (Fe# = {Fe^{3+}/(Fe^{3+} + Cr + Al)} molar ratio) varied from 0.003 to 0.041 and 0.04 to 0.052, respectively. The inclusions of chromite grains in the ultramafics did not show any compositional variations from the core to the rim. All the data considered for the present research are chromite core compositions.

4.3.2. Orthopyroxene

Orthopyroxenite in the Kaliapani area contained enstatite ($En_{90.4}$ to $En_{90.7}$) (Figure 3f). Enstatite has a low Al_2O_3 content (0.68–0.80 wt %), with low CaO (0.60 to 0.76 wt%) and TiO_2 contents (<0.06 wt%). Cr_2O_3 content ranges from 0.51 to 0.67 wt%. The Cr# [Cr/(Cr + Al) molar ratio] and Mg# [Mg/Mg + Fe^{2+}molar ratio] contents of enstatite in orthopyroxenite vary from 0.30 to 0.37and 0.91 to 0.92, respectively.

4.3.3. Olivine

The analyses of the olivine obtained from dunite showed it was high in magnesium (MgO 48.96 to 51.40 wt%) and low in Al_2O_3 (<0.05 wt%), CaO (<0.17 wt%), TiO_2, and Cr_2O_3 (all the samples showed trace concentrations). The olivines in the dunites were identified as forsterite, and the forsterite concentration varied from $Fo_{90.9}$ to $Fo_{94.1}$.

5. Discussion

5.1. Role of Crustal Contamination

To comprehend the petrogenesis and tectonic contexts of the Sukinda ultramafic rocks, assessing the potential influence of crustal components on their composition was crucial. Throughout the phases of mantle melting, magma ascent, and temporary lodgment of melts, there was a chance of incorporating crustal elements into the magma, especially within a continental environment [53,54]. Nevertheless, the Sukinda ultramafic rocks exhibited substantial levels of Mg# (averaging 84 wt%), Ni (averaging 1709 ppm), Cr (averaging 15,050 ppm), V (averaging 71.5 ppm), and Sc (averaging 8 ppm), alongside diminished concentrations of Al_2O_3 (averaging 1.67 wt%), Na_2O (averaging 0.16 wt%), K_2O (occurring in trace amounts), and TiO_2 (averaging 0.05 wt%). These compositional characteristics provided no indication of potential crustal influence or contamination within the Sukinda ultramafic rocks.

Notably, crustal materials are typically enriched in LILEs and LREEs and depleted in Nb, Ta, and Ti [55]. Minor crustal contamination in the magma can manifest as a negative Nb and Ta anomaly; however, it also results in positive Zr and Hf anomalies in adjacent elements [56]. In the primitive mantle-normalized multi-element plot (Figure 5), a negative Nb anomaly was observed in the Sukinda ultramafic rocks. Additionally, the enrichment of LREEs in the REE plot suggested some crustal contamination (Figure 5). However, it is important to note that this geochemical evidence is not unique to crustal

contamination alone. Similar signatures are also evident in mantle-derived boninite and norite magmas, contradicting the presumption of crustal contamination within the parent magma [57–61]. The enrichment of LREEs can potentially occur from certain processes, such as the subduction of continental or oceanic materials into the mantle or metasomatism of the mantle.

If the Sukinda ultramafic rocks underwent crustal contamination, a positive Zr and Hf anomaly would have been observed in the primitive mantle-normalized multi-element plot (Figure 5). Crustally contaminated rock samples usually exhibit disturbed REEs and spider plot patterns, while Sukinda ultramafic rocks display a parallel to sub-parallel pattern (Figure 5). Moreover, the Earth's continental crust is typically enriched in thorium (Th), characterized by higher ratios of Th/La (~0.30) [62] and Th/Ce (~0.15) [63], when compared to magmas originating from the Earth's mantle. These ratios are around ~0.12 for Th/La and 0.02–0.05 for Th/Ce in mantle-derived magmas [64]. In contrast, the Sukinda ultramafic samples exhibited Th/La and Th/Ce ratios averaging 0.18 and 0.09, respectively. These values suggest that there is no evidence of significant crustal contamination during the process of magmatic evolution in Sukinda ultramafic rocks.

5.2. Classification and Parent Melt Composition

Cr-spinel (chromite) occurs as the primary mineral phase in chromitite and as an accessory mineral phase in several mafic-ultramafic litho-types [51,65–67]. Chromite ore deposits are genetically linked to mafic–ultramafic magmatism occurring in particular period and tectonic settings (10, 11), and the chromite chemistry reflects the composition of parent magma. Chromites are considered as the earliest phase to crystalize from mafic–ultramafic magma and are used to determine the primary magma/melt composition. Therefore, the geochemical signature of chromites is widely used to understand the genesis of parent magmas and the tectonic settings of the host rock [65,68–75].

Various authors [68,74,76,77] have established a link between chromite's Al_2O_3 and TiO2 contents and the composition of the surrounding melt. Ref. [77] proposed the idea that Al_2O_3 and TiO_2 contents within chromite remain unaltered, even in the presence of subsolidus re-equilibration with olivine or post-cumulus reactions. As a result, these particular components can be relied upon as consistent indicators for deciphering the geochemical composition of the melt from which the chromite originally crystallized. Ref. [68] pointed out this relationship by studying chromite–olivine and melt inclusion–chromite pairs in oceanic arc and intraplate tectonic settings. The study revealed that the Al_2O_3 and TiO_2 components could be effectively utilized to determine the tectonic setting in which the chromite formed.

In order to determine the Al_2O_3 and TiO_2 chromite–parent melt relationship of Sukinda ultramafics, a set of equations was formulated by [78] using the data of ref. [68]; the TiO_2 and Al_2O_3 contents of spinels (chromites) were exclusively the function of TiO_2 and Al_2O_3 in the melt. The best-fit logarithmic expression for the (Al_2O_3) spinel versus (Al_2O_3) melt and the power regression line for (TiO_2) spinel versus (TiO_2) melt were used to estimate the Al_2O_3 and TiO_2 contents of the parent melt. The spinel–melt compositional relationship is generally used in petrogenetic studies due to its independence from temperature variations or post-cumulus reactions between olivine and chromite. The equations for the (TiO_2) and (Al_2O_3) melts are as follows:

$$Al_2O_3 \text{ wt\% in melt} = 5.356 \ln (Al_2O_3) \text{ wt\% in spinel} - 1.7852 \quad (1)$$

$$TiO_2 \text{ wt\% in melt} = 1.1993(TiO_2 \text{ wt\% in chromite})^{0.8259} \quad (2)$$

The calculated Al_2O_3 wt% melt ranged from 9.93 to 12.54 wt% (Avg. 11.04 wt%) for KLPN samples and 11.21 to 12.86 wt% (Avg. 11.95 wt%) for KTPL samples. The calculated TiO_2 wt% in the melt ranged from 0.20 to 0.31 wt%. (Avg. 0.27 wt%) for KLPN and 0.26 to 0.44 wt% (Avg. 0.35 wt%) for KTPL samples. The calculated values of (Al_2O_3) and (TiO_2) melts indicated a boninitic affinity of the parent melt (Figure 6a). These calculated

values are also comparable to boninites in the SSZ setting (Al_2O_3 = 10.06–14.41 wt%, TiO_2 = 0.10–0.52 wt%) [10,72,79–81]. The calculated parental melt of the Sukinda chromites and chemical characteristics of boninites in the Sukinda complex were compared with the other Archean–Paleoproterozoic mafic–ultramafic magmas in the Peninsular Indian shield and are presented in Table S3.

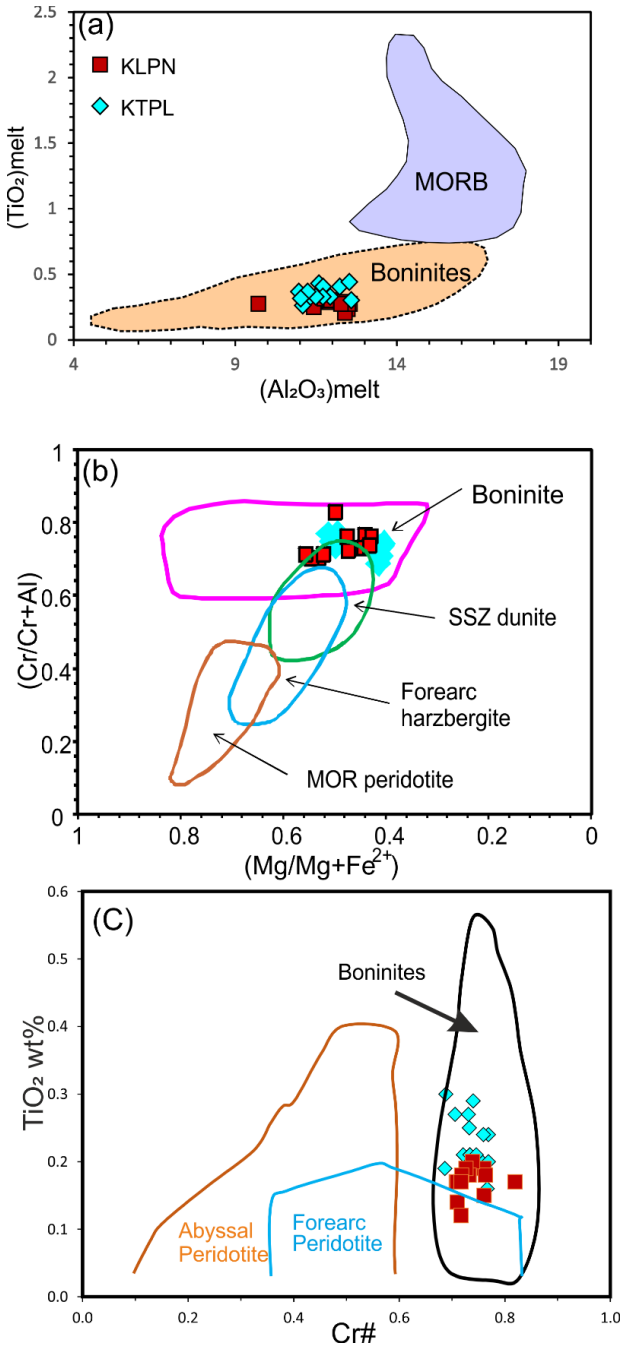

Figure 6. (**a**) Calculated TiO_2 vs. Al_2O_3 composition of melt that was in equilibrium with chromites from the Sukinda complex compared with MORB [82,83] and boninitic compositions [57,84]. (**b**) Mg# (Mg/Mg + Fe^{2+}) vs. Cr# (Cr/Cr + Al) diagram for spinels from Sukinda ultramafic rocks. Fields are drawn after [85–88]. (**c**) The compositional plot of TiO_2 vs. Cr# showing Sukinda ultramafics indicates a boninite affinity. The general boninite field taken after [88–92], the abyssal peridotite field taken after [67,87] and the forearc peridotite field taken after [85,93].

The Mg number (Mg/Mg + Fe^{2+}) versus Cr number (Cr/Cr + Al) plots are presented in Figure 6b (field of forearc harzburgites/peridotites and SSZ dunites were obtained from [85,86,92]). The abyssal peridotite field was obtained from [87] and the boninite field was from [93]), depicting that the chromites fell within the boninite field. In the geochemical plot of TiO_2 versus the Cr number (Figure 6c), all the chromites showed a boninitic parentage. The TiO_2 wt% and Al_2O_3 wt% in the melt of the Sukinda samples were comparable with the Singhbhum boninitic melt composition (Table S2).

The Sukinda ultramafic rocks are characterized by high Mg-olivine (Fo 90.5–94.1), Mg-orthopyroxene (En 90.4–90.7), and Cr-chromite (cr# 68–82) contents. Orthopyroxenes also showed a low aluminum content (Al_2O_3 = 0.68–0.80 wt%). This assemblage is typical of a boninite melt [94]. A highly fractionated PGE pattern of Sukinda chromites, demonstrated by Page et al. [22], and crystallization from S-undersaturated magmas [95] are features of boninitic magmas [96,97].

The mineral chemistry data of olivine, orthopyroxene, chromite, TiO_2 and Al_2O_3 melt calculation, and from previous studies strongly suggest that Sukinda ultramafic rocks derive from a boninitic parent magma.

Sukinda ultramafic rocks are primarily composed of dunites, partially serpentinized dunites, and pyroxenites. During the ultramafic rocks' residence and evolution process, Na_2O, K_2O, and large ion lithophile elements (LILs) (K, Sr, Cs, Rb, Ba) were possibly mobilized and did not reflect their initial distributions. Hence, high-field-strength elements (HFSEs) (Ti, Zr, Y, Nb, Ta, Hf, Th), REEs, and transitional elements (Cr, Ni, Cs, V) are used to classify the Sukinda ultramafic rocks. On the $(Yb)_{CN}$ vs. $(Dy)_{CN}$ diagram (Figure 7a), the samples occupy the field of boninites; one sample falls within the transition of boninite and island arc tholeiite (IAT) field. The samples from the Sukinda ultramafic complex with low V vs. Ti/1000 contents clustered in the "boninite" field (Figure 7b).

The La/Sm vs. TiO_2 distribution (Figure 7c) was narrow and lay within or close to the Phanerozoic boninite field. In the Ti/V vs. Ti/Sc plot (Figure 7d) (one sample close to the SHMB field), most Sukinda samples were close to the fields of boninite.

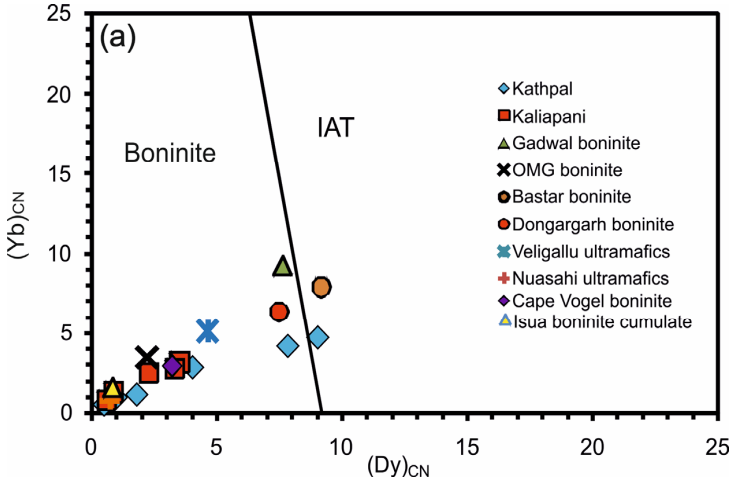

Figure 7. *Cont.*

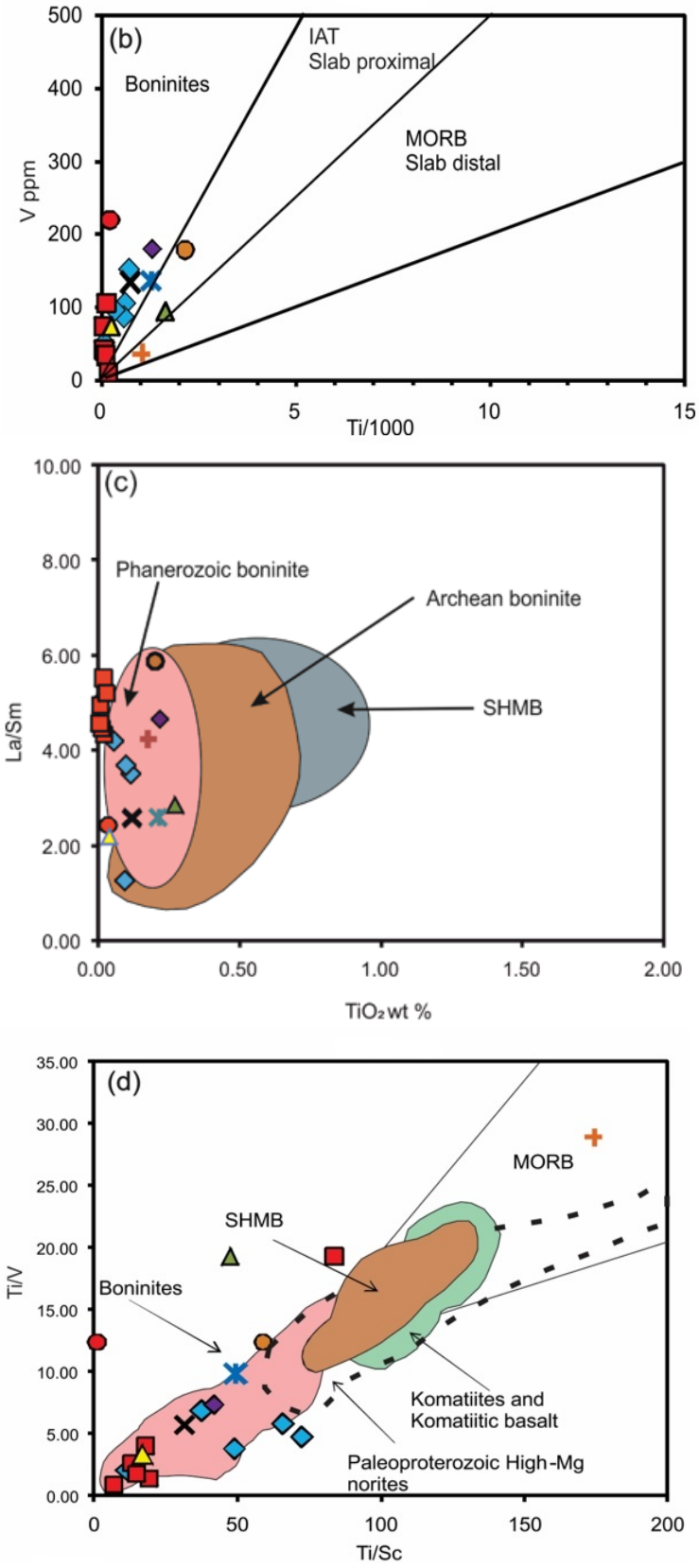

Figure 7. (**a**) $(Yb)_{CN}$ vs. $(Dy)_{CN}$ plot [98] showing distinct fields for boninites and island arc tholeiites (IATs), where most of the Sukinda rock samples cluster in the boninite field. (**b**) Ti/1000 vs. V diagram (after [99]) illustrating the studied samples occupying the fields of boninite. (**c**) La/Sm vs. TiO_2 classification diagram of [58,100,101]. (**d**) Ti/Sc vs. Ti/V diagram for Sukinda ultramafics; the samples occupy the fields of boninites, which differentiate from komatiites, komatiitic basalts, SHMBs, and Palaeoproterozoic

high-Mg norite fields after [54,55,102]. The data of the Sukinda ultramafic complex are plotted along with different high-Mg rocks of the world for comparison purposes. The data are obtained after Gadwal boninite [103]; OMG boninite [46]; Bastar boninite [104]; Dongargarh boninite [105]; Nuasahi ultramafic [9]; Veligallu ultramafics [48]; Cape Vogel boninite [106], and Isua boninite cumulate [52].

5.3. Comparison and Distinction of Sukinda Boninites from Komatiites, Siliceous High-Mg Basalts, Picrites, and Other Ultramafic Formations

Compositional overlaps were seen between boninite, komatiites, siliceous high-Mg basalts, high-Mg norite, and picrite (Table S2). There was a minor geochemical difference between these high-Mg mafic–ultramafic rocks. However, these mafic–ultramafic rocks were identified by their different petrogenesis and distinct geochemical characterization. Geochemically, these high-Mg mafic–ultramafic rocks have high-silica, high-Mg, low-Ti, and low-HFSE levels. Immobile trace-element concentrations, such as Ti, Zr, V, Sc, Yb, and REEs, are essential for discriminating high-Mg mafic–ultramafic rocks, such as boninites and siliceous high-magnesium basalt, komatiites, and picrite [61,107]. The chemical composition of boninite can be recognized by SiO_2 > 53 wt%, its high Mg number (Mg#), Al_2O_3/TiO_2, characteristic U-shaped REE and inclined LREE pattern, and low concentrations of Nb, Ta, and Ti [103].

Higher TiO_2 and lower Al_2O_3 levels chemically characterized picrites and showed an MREE-enriched REE pattern compared to LREE and HREE with positive Zr and Nb anomalies [47]. The plume-generated Archean picrites [108] were characterized by high Nb > 12 ppm contents, Nb/Th > 8 ratio, and positive Nb anomalies. The abovementioned geochemical characterization of picrites was not similar to Sukinda ultramafic rocks.

The high MgO and Mg# concentrations with low Al_2O_3, CaO, and TiO_2 contents and low HFSE (Nb, Zr, Y) and Yb in the Sukinda boninites overlapped with Al-depleted komatiites [109,110]. The high MgO wt% may be due to the second-stage partial melting of a refractory and depleted mantle source [111]. Compared to Bababudan komatiites, the chondrite-normalized rare-earth element pattern showed a depleted LREE and enriched HREE pattern; the negative Nb anomaly observed for the komatiite samples was attributed to the assimilation of lower crustal materials. The Bababudan komatiites also showed positive Zr, Hf, and Ti anomalies on the mantle normalized multi-element diagram, suggesting the derivation of parent magma by melting under anhydrous conditions in the shallow mantle domain, and the garnet entered the melt phase [112].

The Al_2O_3/TiO_2 ratio is the most distinguishing ratio between komatiites and boninites. Komatiites (Al_2O_3/TiO_2 < ~20) are generated by the dry melting of mantle plumes, and boninites (Al_2O_3/TiO_2 > 20) are formed by the wet melting of the refractory mantle wedge in a subduction complex [94,103]. The Katpal samples showed a range of Al_2O_3/TiO_2 ratio range (27.0 to 64.47) and the Kaliapani samples showed a Al_2O_3/TiO_2 ratio range (35.9 to 74.06). Hence, the samples from the Katpal and Kaliapani areas had boninitic characteristics. According to [59,61,94,104,113,114], the Archean komatiites (CaO/Al_2O_3 > 0.85) and Phanerozoic boninites (CaO/Al_2O_3 < 0.85) can be distinguished based on the CaO/Al_2O_3 ratio. The CaO/Al_2O_3 ratio of Kaliapani samples varied from 0.05 to 0.59, and the Katpal samples varied from 0.02 to 0.18 (one sample showed a ratio of 1.24). Hence, the samples were from the Katpal and Kaliapani areas of a Phanerozoic boninite affinity. However, some studies propose that komatiites or komatiitic basalts are the Archean equivalents of boninites and form the partial melting of mantle under hydrous conditions [103,115–117].

Siliceous high-magnesium basalt is another variety of high-Mg rocks found in the Archean–Proterozoic boundary in and around granite greenstone terranes [49]. The genesis of SHMB has different theories: (a) according to [118], SHMBs are the Archean equivalent of modern boninites, (b) SHMBs are the volcanic equivalent of Late Archaean high-Mg norites [59,64], (c) and SHMBs are the products of crustal assimilation and the fractional crystallization (AFC) of komatiite magma, [64,119]. SHMBs and boninites have some

geochemical differences: SHMBs have a low Al_2O_3/TiO_2 and Sc/Y ratio and a high Ti/Zr and Ti/Sc ratio than boninites; however, these two have larger overlapping values [64,120] (Table S2). In comparison to Sonakhan SHMBs (Bastar craton, Manu [72]), the Al_2O_3/TiO_2 (10.18 to 20.71) and Sc/Y (0.23 to 1.16, avg. 0.55) ratios are lower than the Sukinda boninitic rock ratios (Al_2O_3/TiO_2 = 27.0 to 74.06) and (Sc/Y = 0.75 to 11.23 avg. 3.56), and the Ti/Zr (126.4 to 397.3 avg. 218.7) and Ti/Sc (265.8 to 475.3 avg. 372.7) ratios of Sonakhan SHMBs are higher than Sukinda boninitic rock ratios (Ti/Zr = 10.74 to 215.33 avg. 90.37), (Ti/Sc = 7.14 to 83.72 avg. 35.74).

The trace-element and mineral chemistry study shows that Sukinda ultramafic rock is boninitic in nature. Significantly high MgO, Mg#, and low SiO_2 contents do not comply with the standard classification schemes for boninite [113,121]. On the other hand, the high Mg# (78 to 93) content in the Sukinda ultramafics suggests that the rocks may be of a cumulate origin. In contrast, Phanerozoic boninites rarely exceed 18% MgO [106,122,123], and the SiO_2 content in Archean boninites, in contrast to modern boninites, is typically < 52 wt% (e.g., [102,103,120,124,125]. The boninitic rocks in the Singhbhum Craton are characterized by low SiO_2 levels of 42 to 46 wt%, high Mg# levels of 80 to 83 wt%, and MgO levels of 30 to 32 wt% (e.g., [46], and in the Dharwar Craton, the reported boninite composition is characterized by low to medium SiO_2 levels of 45 to 52 wt%, high Mg# levels of 70 to 82 wt%, and MgO levels of 12 to 24 wt%, e.g., [103]). Neoarchean Abitibi greenstone belt boninite rocks show a maximum MgO content of 24.5 wt%, Mg# 83, with a minimum of 44 wt% SiO_2 (Kerrich et al., 1998) [124]. These boninite formations are comparable to Sukinda boninitic rocks. A broader geochemical comparison of different high-Mg mafic rocks and boninites from various Archean and Phanerozoic tectonic settings is presented in Table S2. The Mg# of Sukinda boninite is consistent with boninites from Singbhum (OMG), Dharwar, Bastar, Abitibi, and Isua formations; however, they show higher values than those derived from Archean boninites. The Al_2O_3/TiO_2 ratios for Sukinda boninites conform to Singhbhum (OMG), Bastar, Abitibi, Isua, and Archean boninites, while relatively lower Al_2O_3/TiO_2 ratios characterize Dharwar boninites.

We compared primitive melts from different tectonic settings and Archean–Paleoproterozoic mafic–ultramafic magmas from Peninsular India presented with Sukinda boninitic rocks based on Al_2O_3 and TiO_2 melt contents by the chromite mineral chemistry data (Table S3).

5.4. Petrogenesis of Sukinda Ultramafic Rocks

The generation of boninitic magmatism has been examined by different experimental studies and trace-element modeling. The primary components of boninite magmatism are a high hydroxyl content, higher mantle temperature, and mantle decompression [89,123,126,127]. According to [94,128–130], boninitic magma generation is achieved through a high degree of partial melting, which is metasomatized by slab-derived fluids/melts in a subduction zone at high temperatures (1130–1275 °C) and shallow depths (0.3–1.7 GPa).

The following models were suggested to account for the petrogenesis of boninite magma:

1. Partial melting of serpentinised harzburgite at the time of subduction initiation along a transform fault [131].
2. Subsequent melting of the mantle begins at a mid-oceanic ridge and continues above a subduction zone in response to the addition of water or extension [132,133].
3. Mantle melting is associated with subduction underneath an active or dying oceanic ridge system [93] or beneath a young, hot, oceanic lithosphere [134,135].
4. Partial melting of the mantle wedge in response to the subduction of young, hot, oceanic crust in the early stages of the subduction process [136,137].
5. Partial mantle wedge melting due to the subduction of an active spreading center trending sub-parallel to an intra-oceanic arc-trench system [94].
6. Contact melting of the hydrous mantle wedge due to the introduction of a hot mantle diaper during arc rifting [137].

Hence, the two essential factors of boninite magma generation are: (a) the partial melting of the depleted mantle source and (b) the addition of subducted slab components to the mantle wedge.

5.4.1. Partial Melting of the Depleted Mantle Source

Sukinda ultramafic rocks primarily comprise olivine, pyroxene, and chromite with serpentines. The serpentines are the product of the retrograde metamorphism of olivine and pyroxene. The mineralogical composition of unaltered ultramafics from Sukinda indicates that they evolved from a peridotitic source, most likely spinel-harzburgite. HFSEs (Nb, Zr), REEs (Gd, Yb, Y), and transition elements (TI, V, and Sc) are considered insoluble in an aqueous fluid. At the time of the lithosphere subduction, the lithospheric slab melts by flux melting simultaneously with the mantle wedge. These insoluble elements are retained in the subducted slab; therefore, the concentrations of these elements in the mantle wedge are unchanged. Thus, the concentration of these elements in the arc magma is predominantly controlled by the mantle wedge [138–140]. Hence, these elements' concentrations and ratios can be used to demonstrate the nature of the mantle source.

The notably low Ti/V (2.04–6.88, avg. 4.67) and Ti/Sc (11.73–73.33, avg. 47.21) ratios in the Katpal samples and Ti/V (0.83–19.23, avg. 4.93) and Ti/Sc (7.14–83.72, avg. 26.18) ratios in the Kaliapani block relative to the average N-MORB (Ti/V = 29, and Ti/Sc = 190 [94] show that the mantle source of the Sukinda ultramafic rocks is comparatively more depleted than the average N-MORB. The typical, very high MgO concentrations in the Katpal (32.32 to 44.41 wt%; avg. 39.85 wt%) and Kaliapani areas (34.54 to 47.94 wt%; avg. 42.44 wt%) and very low TiO_2 (<0.03 wt%; avg. 0.02 wt %), Al_2O_3 (<1.22 wt%; avg. 0.99 wt%), and CaO (<0.69 wt%; avg. 0.30 wt%) levels in the Kaliapani and Katpal areas (TiO_2 (<0.12; avg. 0.08 wt %), Al_2O_3 (<3.23 wt%; avg. 2.48 wt%), CaO (<3.85 wt%; avg. 0.87 wt%)) suggest that the ultramafic samples were derived from a highly depleted mantle source [80,133]. The high Mg#, Cr, Ni, and low Nb, Zr, and Y concentrations, and their Zr/Y (avg. 1.24) and Nb/Y (avg. 0.07) ratios and negative Nb anomalies relative to the neighboring trace elements (Figure 5) further suggest that the melts are derived from a relatively high-degree partial melting of a depleted peridotitic mantle source. Indeed, boninite magma's genesis needs a depleted upper mantle source by basaltic melt abstraction in single or multiple episodes, which implies that the mantle harzburgite is the source [80,81,132,133].

Several models were considered to demonstrate the mantle's source composition and geochemical stability field from which the residual magma was derived. Dy/Yb ratios can serve as an indicator to differentiate between the spinel and garnet stability domains during the partial melting of the depleted mantle source [141,142]. In general, partial melting within the garnet stability field tends to produce melts with high Dy/Yb ratios (>2.5), while melting within the spinel stability field produces melts with low Dy/Yb ratios (<1.5). Sukinda boninites, on the other hand, have Dy/Yb ratios ranging from 1.11 to 2.99. This suggests that they are formed through mantle-melting conditions, including spinel peridotite facies and garnet peridotite facies. In the Dy/Yb vs. La/Yb diagram (Figure 8a) [143], most of the Kaliapani samples (Dy/Yb = 1.62–2.99) fall in the garnet peridotite facies zone and the Katpal samples (Dy/Yb = 1.1–1.8) fall in the spinel peridotite zone, respectively. A garnet-bearing source is suspected if $(Gd/Yb)_N > 2$ (four samples from Kaliapani and no samples from Katpal show garnet-bearing sources) or $(Tb/Yb)_N > 1.8$ (four samples from Kaliapani and no samples from Katpal show garnet-bearing sources) [144]. In the $(La/Sm)_{CN}$ vs. $(Gd/Yb)_{CN}$ diagram (Figure 8b), Katpal samples show the affinity of a spinel-bearing source and Kaliapani samples from a garnet-bearing one. These relationships constrain the melting depth, and the spinel/garnet limit is between 80 and 90 km. Hence, the Kaliapani samples are generated at a greater depth than the Katpal samples.

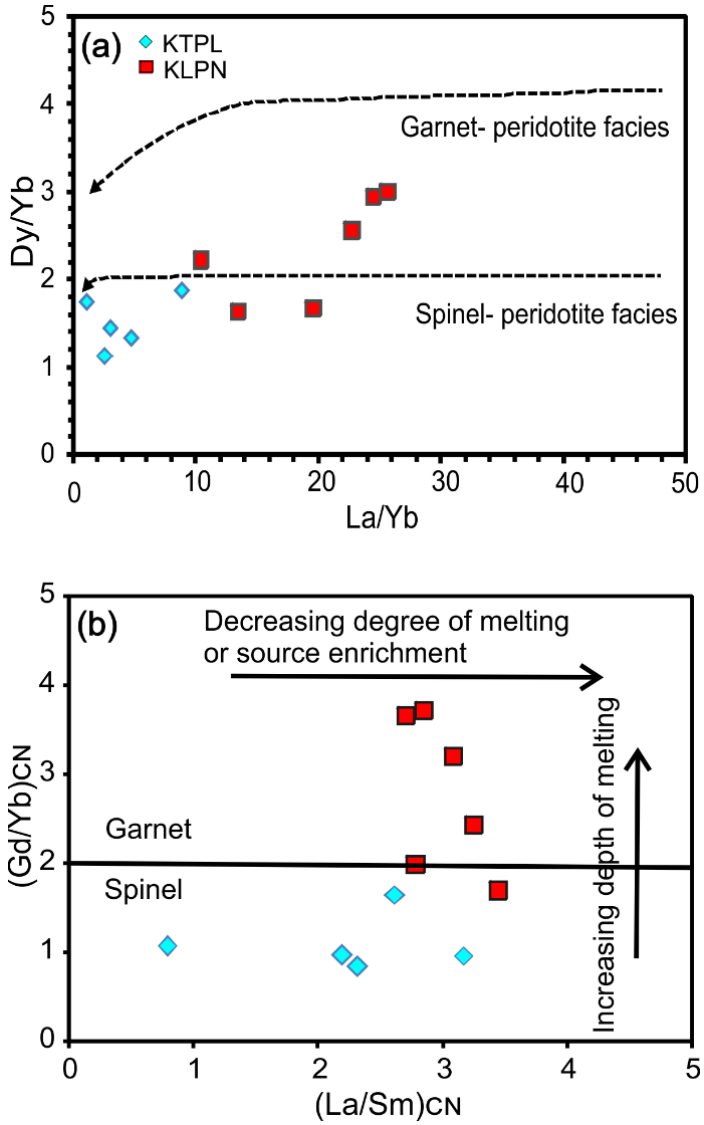

Figure 8. (**a**) Dy/Yb vs. La/Yb diagram [143] suggests mantle melting in spinel peridotite for Sukinda ultramafics. (**b**) $(La/Sm)_{CN}$ vs. $(Gd/Yb)_{CN}$ diagram points to a spinel-bearing source and a garnet-bearing source, and then to a decreasing depth of melting. Normalization values of the chondrite C1 after [40].

5.4.2. Addition of Subducted Slab Components to the Mantle Wedge

The rocks formed in a subduction zone environment start from the early decompression melting of a depleted mantle peridotite to the fluid-fluxed hydrous melting of fertile peridotite mantle that has been remarkably changed by subduction-derived fluids/sediments/melts due to the melting of the subducted slab. The changes are seen in the magma composition, which is regulated by the collaborated effect of melt depletion, metasomatism, enrichment of the mantle wedge by hydrous fluxes, and mantle wedge hybridization by slab melts. This gives rise to tholeiitic forearc basalt in the early stage, followed by the subsequent eruption of boninites, calc-alkaline arc basalts, high-Mg andesites, Nb-enriched basalts, and adakites [145].

During the early subduction process, the hydroxyl components are released from the subducted slab by the dehydration process in shallow mantle conditions and the mantle wedge metasomatism by the addition of slab-derived fluids and water, which leads to boninite magmatism [94,129,130,146]. The boninite magmas are significantly enriched in LILE and LREE compared to HFSE. The Sukinda ultramafics indicate significant

negative anomalies at Nb, Ta, Zr, Hf, and Ti on primitive mantle-normalized trace-element plots (Figure 5), which suggests a significant LILE enrichment relative to the HFSE in the mantle. This significant characteristic feature suggests the infiltration of hydrous fluid from the slab into the mantle source from where the boninite melt is formed [94,129,147–150]. During the flux melting of the subduction slab, the mobile elements, i.e., LREEs and LILEs, are released from the slab and added to the mantle wedge; however, the high-field-strength elements, due to their immobile nature, are retained in the dehydrated slab in a subduction regime [106,129,150]. The released fluid from the subducted slab promotes the migration of elements and decreases the melting temperature of the mantle, which contributes to 3%–25% of the melting of the mantle wedge at a depth of 30–50 km and a 1250–1350 °C mantle temperature [151,152]. The enrichment of Th, U, and LILEs (Figure 5), and the LREE values for Katpal and Kaliapani indicate that the parental magma is subsequently metasomatized by the infiltration of subducted fluids and/or melts during the melt generation process.

In summary, we believe that the geochemical characterization of Sukinda boninites is derived from (i) multiple episodes of extraction of basaltic melt from depleted peridotite sources more refractory than residua from MORB generation; (ii) hydrous fluids/melts derived from a subducting slab enriched in incompatible elements (LILE, LREE); and (iii) the flux-induced re-melting of a metasomatized mantle wedge generating boninitic melts. Overall, it appears that boninitic parental magma is derived from a high degree of partial melting of a depleted mantle source in a subduction zone environment. The ultramafic cumulates were formed due to the early removal of cumulus phases, such as chromite, olivine, and orthopyroxene, during fractional crystallization of the parental boninitic magma.

6. Pressure Condition and Thermal History

The Mg-Fe charge transfer equation between olivine and chromite was used to determine the crystallizing temperature of Sukinda ultramafic rocks. This equation was used as a good geothermometry for chromite-bearing ultramafic rocks [70,153]. In the present study, the forsterite concentration was very high (Fo% = 90 to 94%); therefore, calibration [154] was essential. The thermometry equation is:

$$T^0\ (K) = (4250\ Y^{Sp}{}_{Cr} + 1343)/(\ln K^0{}_D + 1.825 Y^{Sp}{}_{Cr} + 0.571) \quad (3)$$

where $K^0{}_D$ denotes the apparent distribution coefficient $K^0{}_D = \ln K_{D\ -}\ 4.0\ Y^{Sp}{}_{Fe3+}$ [155] $KD = X^{ol}{}_{Mg} X^{Sp}{}_{Fe} / X^{ol}{}_{Mg} X^{sp}{}_{Mg}$ and $Y^{Sp}{}_{Cr} = (Cr/\Sigma \text{ octahedral cations})^{sp}$.

From this equation, the calculated temperature of the Sukinda ultramafic complex ranged from 1258 °C to 1370 °C (average 1329 °C).

The Olivine+chromite+orthopyroxene mineral assemblage indicated the crystallization of rocks with a pressure range of 1 to 2 Gpa, equivalent to pyrolite's melting condition in the spinel peridotite field [87]. The P-T figure (Figure 9) of melting pyrolite [156] indicates the possible crystallization of Sukinda ultramafic rocks at about ~1.7 Gpa and 1300 °C, representing the spinel peridotite field.

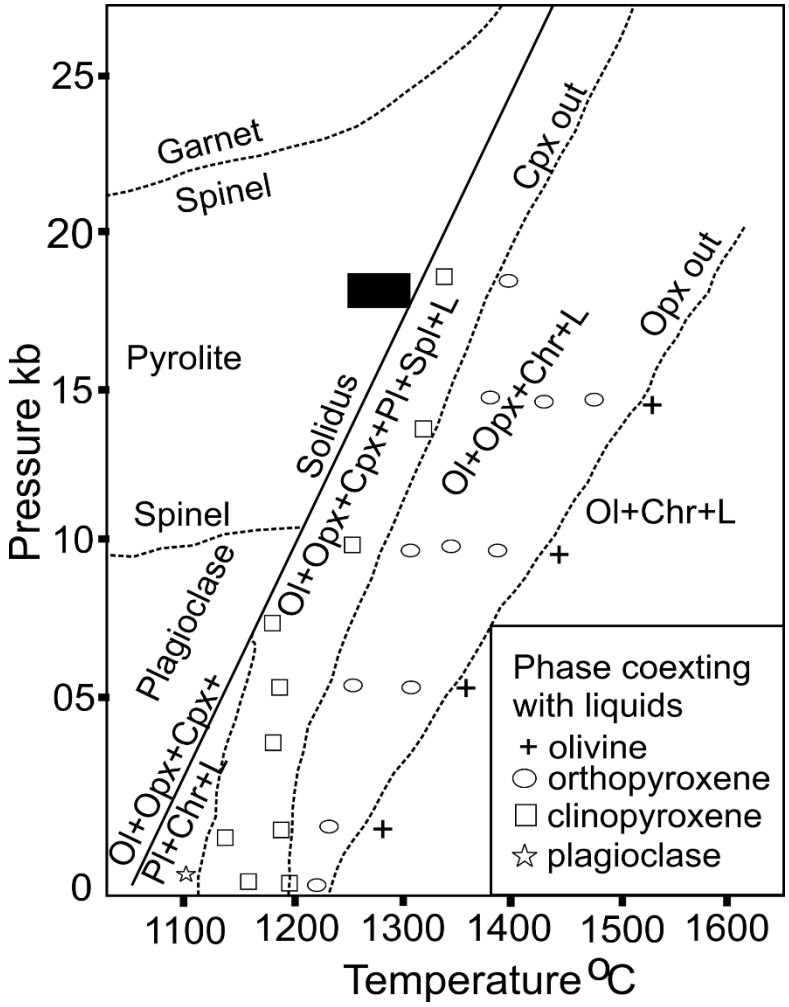

Figure 9. P–T diagram for melting of pyrolite (after [156]).Ol: olivine, Opx: orthopyroxene, Cpx: clinopyroxene, Spl: spinel, Chr: chromite, pl: plagioclase, L: liquid, the rectangular black box indicates the possible pressure condition of Sukinda ultramafic rocks.

7. Tectonic Framework of the Sukinda Complex

The mafic–ultramafic rocks are formed in diverse tectonic environments, such as large layered igneous complexes (stratiform type), subduction allied tectonic settings (Alaskan type), and ophiolites in active orogenic settings (podiform type). The above mentioned varieties of tectonic settings have their characteristic geochemical features, which can be used to recognize the tectonic environment [79,87,157].

A high U/Th ratio (0.48–23.9) and negative Nb-Ta-Ti anomalies in the primitive mantle normalized multi-element diagram indicate the significant role of subduction-related melts/fluids associated with boninite magma genesis. If the mantle plume (komatiitic affinity) mixed up in the genesis of boninites, there would have been a positive Zr anomaly in the multi-element-normalized diagram [127,158–160].

Sukinda ultramafic rocks are characterized by high Mg-olivine (Fo 90–94), high–Mg, and low-Al orthopyroxene (En 90.4–90.7, Al_2O_3 < 0.80 wt %) concentrations, and a high-Cr concentration in chromites (Cr# 68–82) is typical of boninite melts in supra-subduction zone environments [94]. According to [57], boninitic magmas are associated with subduction and arc-related settings, and the bivariant Al_2O_3 versus TiO_2 plots (Figure 10a) indicate that chromites fall in the field of supra-subduction zone peridotites and high-Ti arc settings. The Al_2O_3 versus Fe^{2+}/Fe^{3+} plot (Figure 10b) also suggests chromites are linked to either the supra-subduction zone or volcanic settings. The chromite chemistry of Sukinda ultramafics suggests that chromite host rocks are associated with the SSZ environment, which further

indicates that they are formed during the initial stages of subduction. The evidence from the SSZ rocks suggests that the early formed magma is of a boninitic composition, which is derived in response to the intra-oceanic subduction resulting in the partial melting of the hydrated oceanic lithosphere in the mantle wedge [148,161].

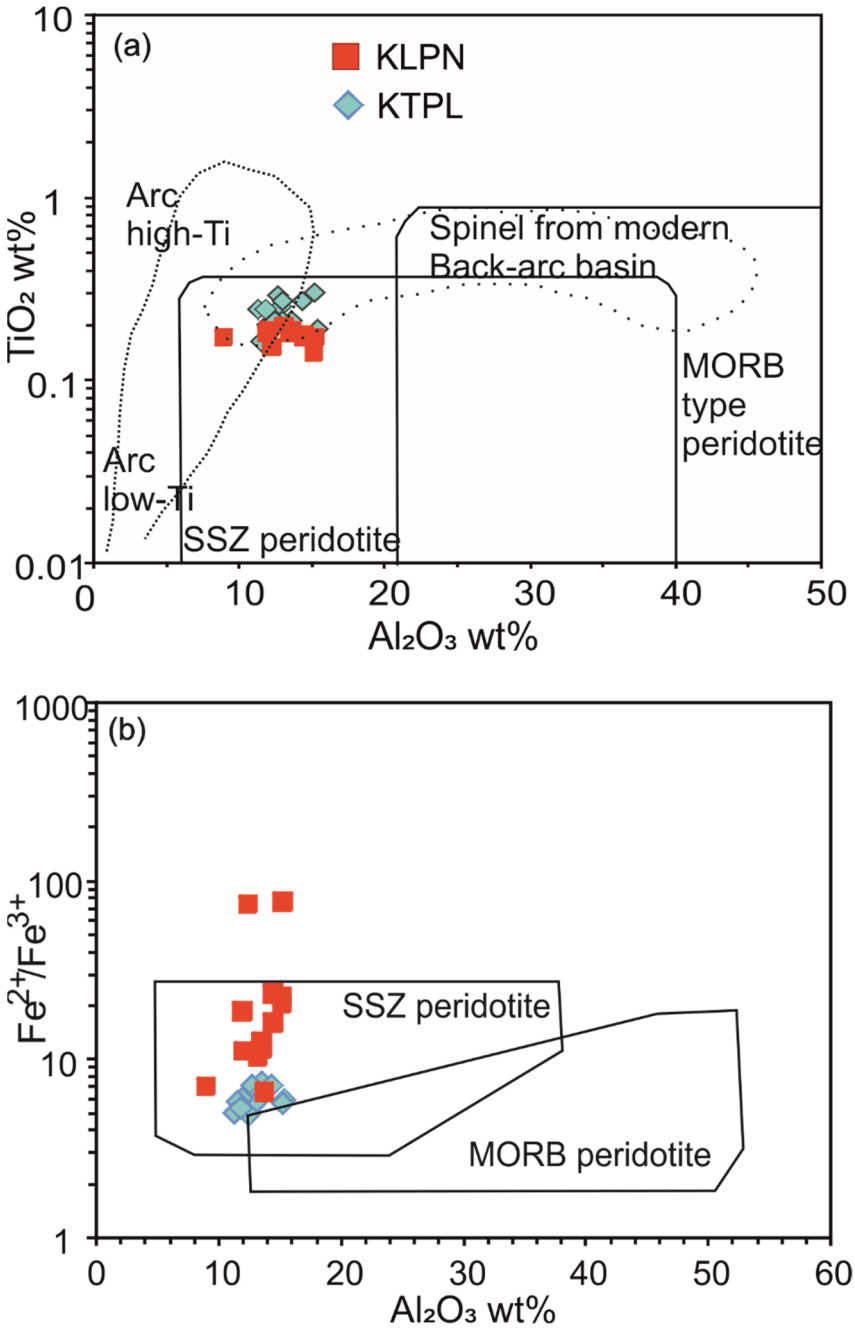

Figure 10. (**a**) TiO_2wt% vs. Al_2O_3wt% and (**b**) Fe^{2+}/Fe^{3+} vs. Al_2O_3 wt% diagram for chrome spinel in Sukinda ultramafics indicate supra-subduction zone tectonic settings; field after [62].

The plausible model, which is schematically shown (Figure 11), can be illustrated and described; Sukinda ultramafics in the Singhbhum Craton are formed from multiple episodes of extraction of basaltic melt from a depleted peridotite source. The mantle wedge generating boninitic melts intrudes further into the iron ore group of rocks in a supra-subduction zone setting. Cumulates of olivine and pyroxene are developed, and chromite mineralization occurs in the intercumulus space in the Sukinda ultramafic complex.

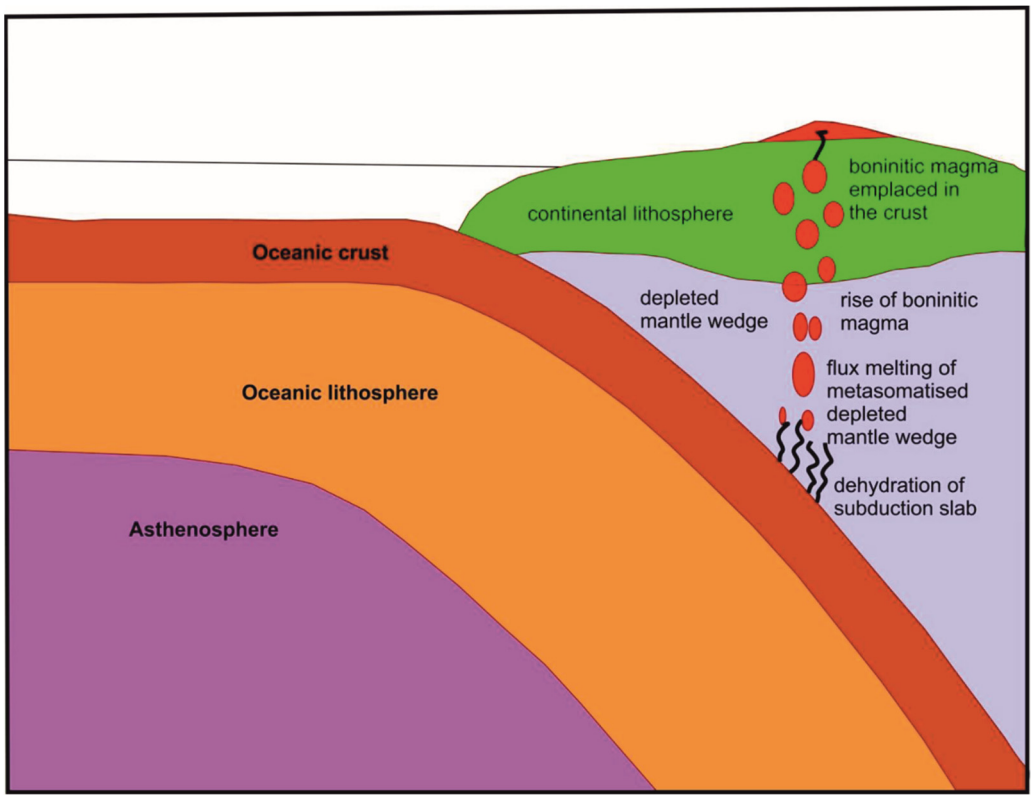

Figure 11. Schematic representation of possible tectonic setting for forming chromiferous ultramafic rocks in the Sukinda complex.

8. Conclusions

The study extensively examined the Sukinda ultramafic complex in the Kaliapani and Katpal areas, encompassing comprehensive petrology, whole-rock geochemistry, and mineral chemistry analyses. The primary conclusions drawn from this research are as follows:

Firstly, the Sukinda ultramafic rocks found within the Singhbhum Odisha Craton exhibit distinctive major and trace-element geochemistry data. By employing melt calculations based on unaltered chromite mineral chemistry data, we ascertained that the original composition of the parent magma responsible for the Sukinda ultramafic complex aligned with a boninitic parentage.

Additionally, the chemical makeup of the chromites within the ultramafic rocks from the Sukinda complex provided compelling evidence that their formation occurred within the context of a supra-subduction zone arc tectonic setting.

Furthermore, the insights achieved from mineral chemistry analyses of Sukinda ultramafics indicate a crystallization temperature of approximately ~1300 °C, as determined through olivine spinel thermometry. This process occurred under a pressure exceeding 1.0 GPa, signifying that the Sukinda ultramafic rocks originated from upper mantle conditions.

Moreover, the ultramafic rocks distinctly exhibited a boninitic affinity, characterized by an enrichment in fluid mobile elements, alongside conspicuous negative anomalies in elements, such as Nb, Zr-Hf, and Ti. These features collectively point towards a genesis process deeply rooted in subduction-related environmental conditions.

Finally, the formation of ultramafic cumulates can be attributed to the early elimination of cumulus phases, such as chromite, olivine, and orthopyroxene. This phenomenon is attributed to the fractional crystallization process of the initial boninitic magma.

Supplementary Materials: The following supporting information can be downloaded at: https://www.mdpi.com/article/10.3390/min13111440/s1, Table S1: Main element oxide contents by

XRF (wt%), trace element and REE contents (ppm, $\mu g \cdot g^{-1}$) by HR-ICP-MS, and relative standard deviations (%RSD) for reference materials JH-1, JB-3, BHVO-1, UB-N. Fe_2O_3T represents total iron content. Certified values from GEOREM (http://georem.mpch-mainz.gwdg.de, accessed on 17 July 2023). Further explanation in text; Table S2: The geochemical comparison of different high-Mg mafic rocks and boninites from various Archean and Phanerozoic tectonic setting [46,58,59,64,102–104,112,124,162,163]; Table S3: Calculated parental melt of the Sukinda ultramafic complex chromites and chemical characteristics of boninites compared with other Archean-Paleoproterozoic mafic-ultramafic magmas of Peninsular India and primitive melts of different tectonic settings [10,35,46,68,75,78,80,86,101,103,104,114,164–176].

Author Contributions: Conceptualization, D.N. and P.D.; methodology, D.N.; software, D.N.; validation, D.N.; formal analysis, D.N.; investigation, D.N., S.M.; resources, D.N.; data curation, D.N.; writing—original draft preparation, D.N.; writing—review and editing D.N., S.M. and P.D.; visualization, D.N., S.M. and P.D.; supervision, D.N. and P.D. All authors have read and agreed to the published version of the manuscript.

Funding: This research work funded by IIT(ISM)-Junior Research Fellowship.

Data Availability Statement: Not applicable.

Acknowledgments: The authors are thankful to the Director of Indian Institute of Technology (Indian School of Mines) Dhanbad, India for the permission to publish the work. TISCO Ltd., FACOR Ltd., and OMC are acknowledged for their help during the fieldwork in the Sukinda areas. DN acknowledges the CRF facility hosted in IIT (ISM), Dhanbad and DST-FIST Level-II. Thanks to the Director of CSIR-NGRI, Hyderabad, for the financial concession in the HR-ICP-MS analysis.

Conflicts of Interest: The authors declare no conflict of interest.

References

1. Zhang, Z.H.; Mao, J.W.; Du, A.D.; Pirajno, F.; Yang, J.M.; Wang, Z.L.; Chai, F.M.; Zhang, Z.C. Re–Os dating of the two largest Cu–Ni sulfide deposits in northern Xinjiang, and its geological significance. *Asian J. Earth Sci.* **2008**, *32*, 204–217. [CrossRef]
2. DeWit, M.J.; Tredoux, M. P.G.E. in the 3.5 Ga Jamestown Ophiolite Complex, Barberton greenstone belt, with implications for P.G.E. distribution in simatic lithosphere. In *Proceedings of the Symposium GeoPlatinum*; Prichard, H.M., Potts, P.J., Bowles, J.F.W., Cribb, S.J., Eds.; Elsevier: London, UK; New York, NY, USA, 1987; Volume 87, pp. 319–341.
3. Naldrett, T.; Kinnaird, J.; Wilson, A.; Chunnett, G. The concentration of P.G.E. in the Earth's crust with special reference to the Bushveld Complex. *Earth Sci. Front.* **2008**, *15*, 264–297. [CrossRef]
4. Song, X.Y.; Zhou, M.F.; Hou, Z.Q.; Cao, Z.M.; Wang, Y.L. Ni-Cu-(P.G.E.) magmatic sulfide deposits in the Yangliuping area, Permian Emeishan igneous province, S.W. China. *Miner. Depos.* **2003**, *38*, 831–843. [CrossRef]
5. Zhu, W.G.; Zhong, H.; Hu, R.Z.; Liu, B.G.; He, D.F.; Song, X.Y.; Deng, H.L. Platinum-group minerals and tellurides from the PGE-bearing Xinjie layered intrusion in the Emeishan Large Igneous Province, SW China. *Mineral. Petrol.* **2010**, *98*, 167–180. [CrossRef]
6. Prendergast, M.D. Archean komatiitic sill-hosted chromite deposits in the Zimbabwe craton. *Econ. Geol.* **2008**, *103*, 981–1004. [CrossRef]
7. Rollinson, H. The Archean komatiite-related Inyala chromitite, southern Zimbabwe. *Econ. Geol.* **1997**, *92*, 98–107. [CrossRef]
8. Stowe, C.W. Chromite deposits of the Shurugwi greenstone belt, Zimbabwe. In *Evolution of Chromium Ore Fields*; Stowe, C.W., Ed.; Hutchinson Ross Publication: New York, NY, USA, 1997; pp. 71–88.
9. Khatun, S.; Mondal, S.K.; Zhou, M.-F.; Balaram, V.; Prichard, H.M. Platinum-group element (P.G.E.) geochemistry of Mesoarchean ultramafic-mafic cumulate rocks and chromitites from the Nuasahi Massif, Singhbhum craton (India). *Lithos* **2014**, *205*, 322–340. [CrossRef]
10. Mondal, S.K.; Ripley, E.M.; Li, C.; Frei, R. The genesis of Archean chromitites from the Nuasahi and Sukinda massifs in the Singhbhum craton, India. *Precambrian Res.* **2006**, *148*, 45–66. [CrossRef]
11. Stowe, C.W. Composition and tectonic settings of chromite deposits through time. *Econ. Geol.* **1994**, *89*, 528–546. [CrossRef]
12. Mondal, S.K. Chromite and P.G.E. deposits of Mesoarchean ultramafic–mafic suites within the greenstone belts of the Singhbhum Craton (India): Implication for mantle heterogeneity and tectonic setting. *J. Geol. Soc. India* **2009**, *73*, 36–51. [CrossRef]
13. Mondal, S.K.; Zhou, M.F. Enrichment of P.G.E. through interaction of evolved boninitic magmas with early formed cumulates in a gabbro-breccia zone of the Mesoarchean Nuasahi Massif (eastern India). *Miner. Depos.* **2010**, *45*, 69–91. [CrossRef]
14. Mukherjee, R.; Mondal, S.K.; Zhong, H.; Bai, Z.-J.; Balaram, V.; Kumar, G.R.R. Platinum-group element geochemistry of komatiite-derived 3.1 Ga ultramafic–mafic rocks and chromitites from the Nuggihalli greenstone belt, western Dharwar craton (India). *Chem. Geol.* **2014**, *386*, 190–208. [CrossRef]

15. Mukherjee, R.; Mondal, S.K.; Gonzalez-Jimenez, J.M.; Griffin, W.L.; Pearson, N.J.; O'Reilly, S.Y. Trace element fingerprints of chromite, magnetite and sulfide from the 3.1 Ga ultramafic-mafic rocks of the Nuggihalli greenstone belt, Western Dharwar Craton (India). *Contrib. Mineral. Petrol.* **2015**, *169*, 59. [CrossRef]
16. Acharyya, S.K. Greenstones from Singhbhum craton, their Archaean character, oceanic crustal affinity and tectonics. *Proc. Nat. Acad. Sci. India Sec.* **1993**, *63*, 211–222.
17. Srinivasachari, K. Stratiform chromite deposits of Sukinda-Nuasahi ultramafic belt, Orissa, India. *Geol. Surv. India Misc. Publ.* **1974**, *34*, 151–160.
18. Mukhopadhyay, D.; Dutta, D.R. Structures in the Roro ultramafics and their country rocks, Singhbhum district, Bihar. In *Structure and Tectonics of Precambrian Rocks of India*; Recent Researches in Geology; Hindustan Publishing Corporation: New Delhi, India, 1983; Volume 10, pp. 98–109.
19. Basu, A.; Maitra, M.; Roy, P.K. Petrology of mafic-ultramafic complex of Sukinda Valley Odisha. *Indian Miner.* **1997**, *50*, 271–290.
20. Chakraborty, K.L.; Chakraborty, T.L. Geological features and origin of the chromite deposits of SukindaValley, Odisha, India. *Miner. Depos.* **1984**, *19*, 256–265. [CrossRef]
21. Pal, T.; Mitra, S. P-T-fO_2 controls on a partly inverse chromite bearing ultramafic intrusive: An evaluation from the Sukinda Massif, India. *J. Asian Earth Sci.* **2004**, *22*, 483–493. [CrossRef]
22. Page, N.J.; Banerji, P.K.; Haffty, J. Characterization of the Sukinda and Nausahi ultramafic complexes, Orissa, India by platinum-group element geochemistry. *Precambrian Res.* **1985**, *30*, 27–41. [CrossRef]
23. Misra, S.; Deomurari, M.P.; Wiedenbeck, M.; Goswami, J.N.; Ray, S.; Saha, A.K. $^{207}Pb/^{206}Pb$ zircon ages and the evolution of the Singhbhum Craton, eastern India: An ion microprobe study. *Precambrian Res.* **1999**, *93*, 139–151. [CrossRef]
24. Saha, A.K.; Ray, S.L.; Sarkar, S.N. Early history of the Earth: Evidence from the eastern Indian Shield. *Geol. Soc. India Mem.* **1988**, *8*, 13–37.
25. Sarkar, S.N.; Saha, A.K. Structure and tectonics of the Singhbhum-Orissa iron ore craton, eastern India. In *Structure and Tectonics of the Precambrian Rocks*; Sinha-Roy, S., Ed.; Recent Researches in Geology; Hindustan Publ. Co.: Delhi, India, 1983; Volume 10, pp. 1–25.
26. Saha, A.K. Crustal evolution of Singhbhum North Odisha, Eastern India. *Geol. Soc. India Mem.* **1994**, *27*, 341.
27. Mukhopadhyay, D. The Archean nucleus of Singhbhum: The present state of knowledge. *Gondwana Res.* **2001**, *4*, 307–318. [CrossRef]
28. Misra, S. Precambrian chronostratigraphic growth of Singhbhum–Orissa Craton, Eastern Indian Shield: An alternative model. *J. Geol. Soc. India* **2006**, *67*, 356–378.
29. Mondal, S.K.; Khatun, S.; Prichard, H.M.; Satyanarayanan, M.; Kumar, G.R.R. Platinum-group element geochemistry of boninite-derived Mesoarchean chromitites and ultramafic-mafic cumulate rocks from the Sukinda Massif (Orissa, India). *Ore Geol. Rev.* **2019**, *104*, 722–744. [CrossRef]
30. Mukhopadhyay, J.; Beukes, N.J.; Armstrong, R.A.; Zimmermann, U.; Ghosh, G.; Medda, R.A. Dating the oldest greenstone in India: A 3.51-Ga precise U–Pb SHRIMP zircon age for dacitic lava of the Southern Iron Ore Group, Singhbhum Craton. *J. Geol.* **2008**, *116*, 449–461. [CrossRef]
31. Misra, S.; Johnson, P.T. Geochronological constraints on the evolution of the Singhbhum Mobile Belt and associated basic volcanics of eastern Indian shield. *Gond. Res.* **2005**, *8*, 129–142. [CrossRef]
32. Bose, M.K. Mafic-ultramafic magmatism in the eastern Indian craton—A review. *Geol. Surv. India Spec. Publ.* **2000**, *55*, 227–258.
33. Sengupta, S.; Acharya, S.K.; De Smith, J.B. Geochemistry of Archean volcanic rocks from Iron Ore Supergroup, Singhbhum, eastern India. *Proc. Indian Acad. Sc.* **1997**, *106*, 327–342.
34. Sahu, N.K.; Mukherjee, M.M. Spinifex textured komatiite from BadampaharGorumahishani schist belt, Mayurbhanj district, Orissa. *J. Geol. Soc. India* **2001**, *57*, 529–534.
35. Chaudhuri, T.; Mazumder, R.; Arima, M. Petrography and geochemistry of Mesoarchaean komatiites from the eastern Iron Ore belt, Singhbhum craton, India, and its similarity with "Barberton type komatiite". *J. Afr. Earth Sci.* **2015**, *101*, 135–147. [CrossRef]
36. Chaudhuri, T.; Satish-Kumar, M.; Mazumder, R.; Biswas, S. Geochemistry and Sm-Nd isotopic characteristics of the Paleoarchean Komatiites from Singhbhum Craton, Eastern India and their implications. *Precambrian Res.* **2017**, *298*, 385–402. [CrossRef]
37. Paul, D.; Mukhopadhyay, D.; Pyne, T.; Bishui, P. Rb-Sr age of granitoid in the Deo River Section, Singhbhum and its relevance to the age of iron formation. *Indian Miner.* **1991**, *45*, 51–56.
38. Roy, A.; Sarkar, A.; Jeyakumar, S.; Aggarwal, S.K.; Ebihara, M.; Satosh, H. Late Archean mantle metasomatism below eastern Indian craton: Evidence from trace elements, REE geochemistry and Sr–Nd–O isotope systematics of ultramafic dykes. *Proc. Indian Acad. Sci.* **2004**, *113*, 649–665.
39. Banerjee, P.K. Geology and geochemistry of the Sukinda ultramafic field, Cuttack district, Odisha. *Mem. Geol. Surv. India* **1972**, *103*, 171.
40. McDonough, W.F.; Sun, S.S. The composition of the Earth. *Chem. Geol.* **1995**, *120*, 223–253. [CrossRef]
41. Satyanarayanan, M.; Balaram, V.; Sawant, S.S.; Subramanyam, K.S.V.; Krishna, G.V.; Dasaram, B.; Manikyamba, C. Rapid determination of REEs, P.G.E.s, and other trace elements in geological and environmental materials by high resolution inductively coupled plasma mass spectrometry. *At. Spectrosc.* **2018**, *39*, 1–15. [CrossRef]
42. Droop, G.T.R. A general equation for estimating Fe^{3+} concentrations in ferromagnesian silicates and oxides from microprobe analyses, using stoichiometric criteria. *Mineral. Mag.* **1987**, *51*, 431–435. [CrossRef]

43. Banerjee, M.; Dutta, U.; Anand, R.; Atlas, Z.D. Insights on the process of two-stage coronae formation at olivine-plagioclase contact in mafic dyke from Palghat Cauvery Shear Zone, southern India. *Mineral. Petrol.* **2019**, *113*, 625–649. [CrossRef]
44. Deer, W.A.; Howie, R.A.; Zussman, J. *An Introduction to the Rock-Forming Minerals*, 3rd Excerpted Student ed.; The Mineralogical Society: London, UK, 2013.
45. Humphries, D.W. *The Preparation of Thin Sections of Rocks, Minerals and Ceramics. Royal Microscopical Society*; Oxford University Press, Oxford Science Publication: Oxford, UK; New York, NY, USA, 1992; Volume 24, p. 83.
46. Manikyamba, C.; Ray, J.; Ganguly, S.; Singh, M.R.; Santosh, M.; Saha, A.; Satyanarayana, M. Boninitic metavolcanic rocks and island arc tholeiites from the Older Metamorphic Group (O.M.G.) of Singhbhum craton, eastern India: Geochemical evidence for Archean subduction processes. *Precambrian Res.* **2015**, *271*, 138–159. [CrossRef]
47. Revillon, S.; Arndt, N.T.; Hallot, E.; Kerr, A.C.; Tarney, J. Petrogenesis of picrites from the Caribbean Plateau and the North Atlantic magmatic province. *Lithos* **1999**, *49*, 1–21. [CrossRef]
48. Khanna, T.C.; Sesha Sai, V.V.; Bizimis, M.; Krishna, A.K. Petrogenesis of ultramafics in the Neoarchean Veligallu greenstone terrane, eastern Dharwar craton, India: Constraints from bulk-rock geochemistry and Lu-Hf isotopes. *Precambrian Res.* **2016**, *285*, 186–201. [CrossRef]
49. Peng, T.; Wilde, S.A.; Fan, W.; Peng, B. Neoarchean siliceous high-Mg basalt (SHMB) from the Taishan granite-greenstone terrane, Eastern North China Craton: Petrogenesis and tectonic implications. *Precambrian Res.* **2013**, *228*, 233–249. [CrossRef]
50. Maier, W.D.; Barnes, S.J.; Campbell, I.H.; Fiorentini, M.L.; Peltonen, P.; Barnes, S.-J.; Smithies, R.H. Progressive mixing of meteoritic veneer into the early Earth's deep mantle. *Nature* **2009**, *460*, 620–623. [CrossRef]
51. Rollinson, H.; Appel, P.W.U.; Frei, R. A metamorphosed, early Archaean chromitite from west Greenland: Implications for the genesis of Archaean anorthosite chromitites. *J. Petrol.* **2002**, *43*, 2143–2170. [CrossRef]
52. Szilas, K.; Kelemen, P.B.; Rosing, M.T. The petrogenesis of ultramafic rocks in the >3.7 Ga Isua supracrustal belt, southern West Greenland: Geochemical evidence for two distinct magmatic cumulate trends. *Gondwana Res.* **2015**, *28*, 565–580. [CrossRef]
53. Mohr, P.A. Crustal Contamination in Mafic Sheets: A summary. In *Mafic Dyke Swarms*; Halls, H.C., Fahrig, W.C., Eds.; Special Publication-Geological Association of Canada: St. John's, NL, Canada, 1987; Volume 34, pp. 75–80.
54. Zhu, Y.; An, F.; Tan, J. Geochemistry of hydrothermal gold deposits: A review. *Geosci. Front.* **2011**, *2*, 367–374. [CrossRef]
55. Rudnick, R.L.; Gao, S. Composition of the continental crust. *Treatise Geochem.* **2004**, *3*, 1–64.
56. Zhao, J.J.; Zhou, M.F. Geochemistry of Neoproterozoic mafic intrusions in the Panzhihua district (Sichuan Province, SW China): Implications for subduction-related metasomatism in the upper mantle. *Precambrian Res.* **2007**, *152*, 27–47. [CrossRef]
57. Cameron, W.E.; McCulloch, M.T.; Walker, D.A. Boninite petrogenesis: Chemical and Nd-Sr isotopic constraints. *Earth Planet. Sci. Lett.* **1983**, *65*, 75–89. [CrossRef]
58. Hall, R.P.; Hughes, D.J. Norite dykes of southern Greenland, early Proterozoic boninitic magmatism. *Contrib. Mineral. Petrol.* **1987**, *97*, 169–182. [CrossRef]
59. Hall, R.P.; Hughes, D.J. (Eds.) *Norite Magmatism. Early Precambrian Basic Magmatism*; *Blackie, Glasgow*; Springer: Dordrecht, The Netherlands, 1990; pp. 83–110.
60. Poidevin, J.L. Boninite-like rocks from the Palaeoproterozoic greenstone belt of Bogoin, Central African Republic: Geochemistry and petrogenesis. *Precambrian Res.* **1994**, *68*, 97–113. [CrossRef]
61. Smithies, R.H. Archaeanboninite like rocks in an intracratonic setting. *Earth Planet. Sci. Lett.* **2002**, *197*, 19–34. [CrossRef]
62. Plank, T. Constraints from thorium/lanthanum on sediment recycling at subduction zones and the evolution of the continents. *J. Petrol.* **2005**, *46*, 921–944. [CrossRef]
63. Taylor, S.R.; McLennan, S.M. The geochemical evolution of the continental crust. *Rev. Geophys.* **1995**, *33*, 241–265. [CrossRef]
64. Sun, S.S.; McDonough, W.F. Chemical and isotopic systematics of oceanic basalt: Implication for mantle composition and processes. *Geol. Soc. Lond. Spec. Publ.* **1989**, *42*, 528–548. [CrossRef]
65. Irvine, T.N. Chromian spinel as a petrogenetic indicator. Part I. Theory. *Can. J. Earth Sci.* **1965**, *52*, 648–672. [CrossRef]
66. Arai, S. Chemistry of chromian spinel in volcanic rocks as a potential guide to magma chemistry. *Mineral. Mag.* **1992**, *56*, 173–184. [CrossRef]
67. Arai, S. Characterization of spinel peridotites by olivine-spinel compositional relationships: Review and interpretation. *Chem. Geol.* **1994**, *113*, 191–204. [CrossRef]
68. Kamenetsky, V.; Crawford, A.J.; Meffre, S. Factors controlling chemistry of magmatic spinel: An empirical study of associated olivine, Cr-spinel and melt inclusions from primitive rocks. *J. Petrol.* **2001**, *42*, 655–671. [CrossRef]
69. Irvine, T.N. Chromian spinel as a petrogenetic indicator, Part II. Petrological applications. *Can. J. Earth Sci.* **1967**, *4*, 71–103. [CrossRef]
70. Barnes, S.J. Chromite in komatiites, II. Modification during greenschist to mid-amphibolite facies metamorphism. *J. Petrol.* **2000**, *41*, 387–409. [CrossRef]
71. Arai, S.; Okamura, H.; Kadoshima, K.; Tanaka, C.; Suzuki, S.; Ishimaru, S. Chemical characteristics of chromian spinel in plutonic rocks: Implications for deep magma processes and discrimination of tectonic setting. *Isl. Arc* **2011**, *20*, 125–137. [CrossRef]
72. Wilson, B.M. *Igneous Petrogenesis a Global Tectonic Approach*; Springer Science & Business Media: Dordrecht, The Netherlands, 2007.
73. Nayak, R.; Pal, D.; Chinnasamy, S.S. High-Cr chromitites of the Nidar Ophiolite Complex, northern India: Petrogenesis and tectonic implications. *Ore Geol. Rev.* **2021**, *129*, 103942. [CrossRef]

74. Roeder, P.L.; Campbell, I.H.; Jamieson, H.E. A re-evaluation of the olivine-spinel geothermometer. *Contrib. Mineral. Petrol.* **1979**, *68*, 325–334. [CrossRef]
75. Rollinson, H. The geochemistry of mantle chromitites from the northern part of the Oman ophiolite: Inferred parental melt compositions. *Contrib. Mineral. Petrol.* **2008**, *156*, 273–288. [CrossRef]
76. Hill, R.; Roeder, P. The crystallization of spinel from basaltic liquid as a function of oxygen fugacity. *J. Geol.* **1974**, *82*, 709–729. [CrossRef]
77. Pagé, P.; Barnes, S.J. Using trace elements in chromites to constrain the origin of podiform chromitites in the ThetfordMines Ophiolite, Quebec, Canada. *Econ. Geol.* **2009**, *104*, 997–1018. [CrossRef]
78. Manu Prasanth, M.P.; Hari, K.R.; Chalapathi Rao, N.V.; Hou, G.; Pandit, D. An island arc tectonic setting for the Neoarchean Sonakhan Greenstone Belt, Bastar Craton, Central India: Insights from the chromite mineral chemistry and geochemistry of the siliceous high-Mg basalts (SHMB). *Geol. J.* **2017**, *53*, 1526–1542. [CrossRef]
79. Wilson, M. *Igneous Petrogenesis*; Unwin Hyman: London, UK, 1989; p. 446.
80. Hickey, R.L.; Frey, F.A. Geochemical characteristics of boninite series volcanics: Implications for their source. *Geochim. Et Cosmochim. Acta* **1982**, *46*, 2099–2115. [CrossRef]
81. Sun, S.S.; Nesbitt, R.W. Geochemical regularities and genetic significance of ophiolitic basalts. *Geology* **1978**, *6*, 689–693. [CrossRef]
82. Shibata, T.; Thompson, G.; Frey, F.A. Tholeiitic and alkali basalts from the Mid-Atlantic Ridge at 43° N. *Contr. Mineral. Petrol.* **1979**, *70*, 127–141. [CrossRef]
83. le Roex, A.P.; Dick, H.J.; Gulen, L.; Reid, A.M.; Erlank, A.J. Local and regional heterogeneity in MORB from the Mid-Atlantic Ridge between 54.5° S and 51° S: Evidence for geochemical enrichment. *Geochim. Cosmochim. Acta* **1987**, *51*, 541–555. [CrossRef]
84. Kamenetsky, V.; Sobolev, A.; Eggins, S.; Crawford, A.; Arculus, R. Olivine-enriched melt inclusions in chromites from low-Ca boninites, Cape Vogel, Papua New Guinea: Evidence for ultramafic primary magma, refractory mantle source and enriched components. *Chem. Geol.* **2002**, *183*, 287–303. [CrossRef]
85. Ishii, T.; Robinson, P.T.; Maekawa, H.; Fiske, R. Petrological studies of peridotites from diapiric serpentinites seamounts in the Izu-Ogasawara-Mariana forearc, Leg 125. *Proc. Ocean. Drill. Program Sci. Results* **1992**, *125*, 445–485.
86. Pearce, J.A.; Barker, P.F.; Edwards, S.J.; Parkinson, I.J.; Leat, P.T. Geochemistry and tectonic significance of peridotites from the South Sandwich arc–basin system, South Atlantic. *Contrib. Miner. Pet.* **2000**, *139*, 36–53. [CrossRef]
87. Dick, H.J.B.; Bullen, T. Chromian spinel as a petrogenetic indicator in abyssal and alpine-type peridotites and spatially associated lavas. *Contrib. Mineral. Petrol.* **1984**, *86*, 54–76. [CrossRef]
88. Van Der Laan, S.R.; Arculus, R.J.; Pearce, J.A.; Murton, B.J. Petrography, mineral chemistry, and phase relations of the basement boninite series of Site 786, Izu-Bonin forearc. *Proc. Ocean. Drill. Program Sci. Results* **1992**, *125*, 171–202.
89. Sobolev, A.V.; Danyushevsky, L.V. Petrology and geochemistry of boninites from the north termination of the Tonga Trench: Constraints on the generation conditions of primary high-Ca boninite magmas. *J. Petrol.* **1994**, *35*, 1183–1211. [CrossRef]
90. Cameron, W.E. Petrology and origin of primitive lavas from Troodos ophiolite, Cyprus. *Contrib. Mineral. Petrol.* **1985**, *89*, 239–255. [CrossRef]
91. Umino, S. Magma mixing in boninite sequence of Chichijima, Bonin island. *J. Volcanol. Geotherm. Res.* **1986**, *29*, 125–157. [CrossRef]
92. Parkinson, I.J.; Pearce, J.A. Peridotites of the Izu-Bonin-Mariana forearc (ODP Leg 125) evidence for mantle melting and melt–mantle interactions in a supra-subduction zone setting. *J. Petrol.* **1998**, *39*, 1577–1618. [CrossRef]
93. Van der Laan, S.R.; Flower, M.F.J.; Koster van Groos, A.F. Experimental evidence for the origin of boninites: Near-liquidus phase relations to 7·5 kbar. In *Boninites and Related Rocks*; Crawford, A.J., Ed.; Unwin and Hyman: London, UK, 1989; pp. 112–147.
94. Crawford, A.J.; Falloon, T.J.; Green, D.H. Classification, petrogenesis and tectonic setting of boninites. In *Boninites and Related Rocks*; Crawford, A.J., Ed.; Unwin Hyman: London, UK, 1989; pp. 2–44.
95. Naldrett, A.J.; von Gruenewoldt, G. Association of platinum group elements with chromitite in layered intrusions and ophiolite complexes. *Econ. Geol.* **1989**, *84*, 180–187. [CrossRef]
96. Sun, S.S.; Wallace, D.A.; Hoatson, D.M.; Glikson, A.Y.; Keays, R.R. Use of geochemistry as a guide to platinum group element potential of mafic–ultramafic rocks: Examples from the west Pilbara Block and Halls Creek mobile zone, Western Australia. *Precambrian Res.* **1991**, *50*, 1–35. [CrossRef]
97. Keays, R.R. The role of komatitic and picritic magmatism and Ssaturation in the formation of ore deposits. *Lithos* **1994**, *34*, 1–18. [CrossRef]
98. Dilek, Y.; Furnes, H. Structure and geochemistry of Tethyan ophiolites and their petrogenesis in subduction rollback systems. *Lithos* **2009**, *113*, 1–20. [CrossRef]
99. Shervais, J.W. Ti–V plots and the petrogenesis of modern and ophiolitic lavas. *Earth Planet. Sci. Lett.* **1982**, *59*, 101–118. [CrossRef]
100. Seitz, H.M.; Keays, R.R. Platinum group element segregation and mineralization in a Noritic Ring complex formed from Proterozoic siliceous high magnesium basalt magmas in the Vestfold Hills, Antarctica. *J. Petrol.* **1997**, *38*, 703–725. [CrossRef]
101. Sensarma, S.; Palme, H.; Mukhopadhyay, D. Crust–mantle interaction in the genesis of siliceous high magnesian basalts: Evidence from the early Proterozoic Dongargarh Supergroup, India. *Chem. Geol.* **2002**, *187*, 21–37. [CrossRef]
102. Polat, A.; Hofmann, A.W.; Rosing, M.T. Boninite-like volcanic rocks in the 3.7–3.8 Ga Isua greenstone belt, West Greenland: 914 geochemical evidence for intra-oceanic subduction zone processes in the early Earth. *Chem. Geol.* **2002**, *184*, 231–254. [CrossRef]

103. Manikyamba, C.; Naqvi, S.M.; Rao, D.S.; Mohan, M.R.; Khanna, T.C.; Rao, T.G.; Reddy, G.L.N. Boninites from the Neoarchaean Gadwal greenstone belt, eastern Dharwar craton, India: Implications for Archaean subduction processes. *Earth Planet. Sci. Lett.* **2005**, *230*, 65–83. [CrossRef]
104. Srivastava, R.K. Geochemistry and petrogenesis of Neoarchaeanhigh-Mg low-Ti mafic igneous rocks in an intracratonic setting, Central India craton: Evidence for boninite magmatism. *Geochem. J.* **2006**, *40*, 15–31. [CrossRef]
105. Chalapathi Rao, N.V.; Srivastava, R.K. A new find of boninite dyke from the Palaeoproterozoic Dongargarh Supergroup: Inference for a fossil subduction zone in the Archaean of the Bastar Craton, Central India. *Neues Jahrb. Für Mineral. Abh.* **2009**, *186*, 271–282.
106. Konig, S.; Munker, C.; Schuth, S.; Luguet, A.; Hoffmann, J.E.; Kuduon, J. Boninites as windows into trace element mobility in subduction zones. *Geochim. Cosmochim. Acta* **2010**, *74*, 684–704.
107. Rollinson, H.R. *Using Geochemical Data: Evaluation, Presentation, Interpretation*; John Wiley: Chichester, UK, 1993; p. 352.
108. Kitayama, Y.C.; Francis, D. Iron-rich alkaline magmatism in the Archean Wawa greenstone belts (Ontario, Canada). *Precambrian Res.* **2014**, *252*, 53–70. [CrossRef]
109. Puchtel, I.S.; Haase, K.M.; Hofmann, A.W.; Chauvel, C.; Kulikov, V.S.; Garbe-Schonberg, C.D.; Nemchin, A.A. Petrology and geochemistry of crustally contaminated komatiitic basalts from the Vetreny belt, southeastern Baltic Shield: Evidence for an early Proterozoic mantle plume beneath rifted Archean continental lithosphere. *Geochim. Cosmochim. Acta* **1997**, *61*, 1205–1222. [CrossRef]
110. Puchtel, I.S.; Hofmann, A.W.; Amelin, Y.V.; Garbe-Schonberg, C.D.; Samsonov, A.V.; Shchipansky, A.A. Combined mantle plume–island arc model for the formation of the 2.9 Ga Sumozero-Kenozero greenstone belt, S.E. Baltic Shield: Isotope and trace element constraints. *Geochim. Cosmochim. Acta* **1999**, *63*, 3579–3595. [CrossRef]
111. Szilas, K.; Naeraa, T.; Schersten, A.; Stendal, H.; Frei, R.; van Hinsberg, V.J.; Kokfelt, T.F.; Rosing, M.T. Origin of Mesoarchean arc-related rocks with boninite/komatiite affinities from south West Greenland. *Lithos* **2012**, *144*, 24–39. [CrossRef]
112. Saha, A.; Manikyamba, C.; Santosh, M.; Ganguly, S.; Khelen, A.C.; Subramanyam, K.S.V. Platinum Group Elements (P.G.E.) geochemistry of komatiites and boninites from Dharwar Craton, India: Implications for mantle melting processes. *J. Asian Earth Sci.* **2015**, *105*, 300–319.
113. Le Bas, M.J. IUGS reclassification of the high-Mg and picritic volcanic rocks. *J. Petrol.* **2000**, *41*, 1467–1470. [CrossRef]
114. Srivastava, R.K. Global IntracratonicBoninite- Norite magmatism during the Neoarchean—Paleoproterozoic: Evidence from the Central Indian Bastar craton. *Int. Geol. Rev.* **2008**, *50*, 61–74. [CrossRef]
115. Parman, S.; Dann, J.; Grove, T.L.; De Wit, M.J. Emplacement conditions of komatiite magmas from the 3.49 Ga Komati formation, Barberton Greenstone Belt, South Africa. *Earth Planet. Sci. Lett.* **1997**, *150*, 303–323.
116. Parman, S.W.; Grove, T.L.; Dann, J.C. The production of Barberton komatiites in an Archean subduction zone. *Geophys. Res. Lett.* **2001**, *28*, 2513–2516.
117. Grove, T.L.; Parman, S.W.; Dann, J.C. Conditions of magma generation for Archean komatiites from the Barberton Mountainland, South Africa. *Spec. Publ. Geochem. Soc.* **1999**, *6*, 155–167.
118. Redman, B.A.; Keays, R.R. Archaean basic volcanism in the Eastern GoldfieldsProvince, Yilgarn Block, Western Australia. *Precambrian Res.* **1985**, *30*, 113–152.
119. Arndt, N.T.; Brügmann, G.E.; Lehnert, K.; Chauvel, C.; Chappell, B.W. Geochemistry, Petrogenesis and Tectonic Environment of Circum-Superior Belt Basalts, Canada. *Geol. Soc. Spec. Publ.* **1987**, *33*, 133–145.
120. Smithies, R.H.; Champion, D.C.; Sun, S.S. The case for Archaean boninites. *Contrib. Mineral. Petrol.* **2004**, *147*, 705–721.
121. Verma, S.P.; Torres-Alvarado, I.S.; Sotelo-Rodr'ıguez, Z.T. SINCLAS: Standard igneous norm and volcanic rock classification system. *Comput. Geosci.* **2002**, *28*, 711–715.
122. Brown, A.V.; Jenner, G.A. Geological setting, petrology and chemistry of Cambrian boninite and low-Ti tholeiitic lavas in western Tasmania. In *Boninites and Related Rocks*; Crawford, A.J., Ed.; Unwin Hyman: London, UK, 1989; pp. 233–263.
123. Xia, X.; Song, S.; Niu, Y. Tholeiite–Boninite terrane in the North Qilian suture zone: Implications for subduction initiation and back-arc basin development. *Chem. Geol.* **2012**, *328*, 259–277.
124. Kerrich, R.; Wyman, D.A.; Fan, J.; Bleeker, W. Boninite series: Low Ti–tholeiite associations from the 2.7 Ga Abitibi greenstone belt. *Earth Planet. Sci. Lett.* **1998**, *164*, 303–316.
125. Boily, M.; Dion, C. Geochemistry of boninite-type volcanic rocks in the Frotet-Evans greenstone belt, Opaticasubprovince, Quebec: Implications for the evolution of Archaean greenstone belt. *Precambrian Res.* **2002**, *115*, 349–371. [CrossRef]
126. Umino, S.; Kushiro, I. Experimental studies on boninite petrogenesis. In *Boninites and Related Rocks*; Crawford, A.J., Ed.; Unwin Hyman: London, UK, 1989; pp. 89–111.
127. Falloon, T.J.; Danyushevsky, L.V. Melting of refractory mantle at 1.5, 2 and 2.5 GPa under anhydrous and H_2O-undersaturated conditions: Implications for high-Ca boninites and the influence of subduction components on mantle melting. *J. Petrol.* **2000**, *41*, 257–283. [CrossRef]
128. Defant, M.J.; Drummond, M.S. Derivation of some modern arc magmas by melting of young subducted lithosphere. *Nature* **1990**, *347*, 662–665. [CrossRef]
129. Pearce, J.A.; Vander Laan, S.R.; Arculus, R.J.; Murton, B.J.; Ishii, T.; Peate, D.W.; Parkinson, I.J. Boninite and harzburgite from Leg 125 (Bonin-Mariana forearc): A case study of magma genesis during the initial stages of subduction, in Fryer. In *Proceeding of the Ocean Drilling Program Scientific Results*; Ocean Drilling Program: College Station, TX, USA, 1992; Volume 125, pp. 623–659.

130. Li, C.; Ripley, E.M.; Thakurta, J.; Stifter, E.C.; Qi, L. Variations of olivine Fo–Ni contents and highly chalcophile element abundances in arc ultramafic cumulates, southern Alaska. *Chem. Geol.* **2013**, *351*, 15–28.
131. Hawkins, J.W.; Bloomer, S.H.; Evans, C.A.; Melchior, J.T. Evolution of intra-oceanic arc-trench systems. *Tectonophysics* **1984**, *102*, 175–205.
132. Duncan, R.A.; Green, D.H. Role of multistage melting in the formation of oceanic crust. *Geology* **1980**, *8*, 22–26. [CrossRef]
133. Duncan, R.A.; Green, D.H. The genesis of refractory melts in the formation of oceanic crust. *Contrib. Mineral. Petrol.* **1987**, *96*, 326–342.
134. Shiraki, K.; Kuroda, N.; Maruyama, S.; Urano, H. Evolution of the Tertiary volcanic rocks in the Izu Mariana Arc. *Bull Volcanol* **1978**, *41*, 548–562. [CrossRef]
135. Meijer, A. Primitive arc volcanism and a boninite series: Examples from western Pacific Island arcs. The tectonic and geologic evolution of Southeast Asian seas and islands. *Wash. DC Am. Geophys. Union Geophys. Monogr. Ser.* **1980**, *23*, 269–282.
136. Tatsumi, Y.; Lshizaka, K. High magnesian andesite and basalt from Shodo-Shima island, south west Japan, and their bearing on the genesis of calc-alkaline andesites. *Lithos* **1982**, *15*, 161–172. [CrossRef]
137. Crawford, A.J.; Beccaluva, L.; Serri, G.; Dostal, J. Petrology, geochemistry and tectonic implications of volcanic dredged from the intersection of the Yap and Mariana trenches. *Earth Planet. Sci. Lett.* **1986**, *80*, 265–280. [CrossRef]
138. Pearce, J.A.; Parkinson, I.J. Trace element models for mantle melting: Application to volcanic arc petrogenesis. *Geol. Soc. Lond. Spec. Publ.* **1993**, *76*, 373–403. [CrossRef]
139. Woodhead, J.; Eggins, S.; Gamble, J. High field strength and transition element systematics in island arc and back-arc basin basalts: Evidence for multi-phase melt extraction and a depleted mantle wedge. *Earth Planet. Sci. Lett.* **1993**, *114*, 491–504. [CrossRef]
140. Elliott, T.; Plank, T.; Zindler, A.; White, W.; Bourdon, B. Element transport from slab to volcanic front at the Mariana arc. *J. Geophys. Res. Solid Earth* **1997**, *102*, 14991–15019. [CrossRef]
141. Jiang, Y.H.; Jiang, S.Y.; Dai, B.Z.; Liao, S.Y.; Zhao, K.D.; Ling, H.F. Middle to late Jurassic felsic and mafic magmatism in southern Hunan province, southeast China: Implications for a continental arc to rifting. *Lithos* **2009**, *107*, 185–204. [CrossRef]
142. Yang, Q.Y.; Santosh, M.; Shen, J.F.; Li, S.R. Juvenile vs. recycled crust in N.E. China: Zircon U–Pb geochronology, Hf isotope and an integrated model for Mesozoic gold mineralization in the Jiadong Peninsula. *Gondwana Res.* **2014**, *25*, 1445–1468. [CrossRef]
143. Rajesh, H.M.; Chisonga, B.C.; Shindo, K.; Beukes, N.J.; Armstrong, R.A. Petrographic, geochemical and SHRIMP U–Pb titanite age characterization of the Thabazimbi mafic sills: Extended time frame and a unifying petrogenetic model for the Bushveld Large Igneous Province. *Precambrian Res.* **2013**, *230*, 79–102. [CrossRef]
144. Rooney, T.O. Geochemical evidence of lithospheric thinning in the southern Main Ethiopian Rift. *Lithos* **2010**, *117*, 33–48. [CrossRef]
145. Stern, R.J.; Reagan, M.; Ishizuka, O.; Ohara, Y.; Whattam, S. To understand subduction initiation, study forearc crust; to understand forearc crust, study ophiolites. *Lithosphere* **2012**, *4*, 469–483. [CrossRef]
146. Hall, R. Cenozoic geological and plate tectonic evolution of SE Asia and the SW Pacific: Computer-based reconstructions, model and animations. *J. Asian Earth Sci.* **2002**, *20*, 353–431. [CrossRef]
147. Pearce, J.A. Trace element characteristics of lavas from destructive plate boundaries. In *Andesites*; Thorpe, R.S., Ed.; Wiley: New York, NY, USA, 1982; pp. 525–548.
148. Pearce, J.A.; Lippard, S.J.; Roberts, S. Characteristics and tectonic significance of supra-subduction zone ophiolites. *Geol. Soc. Spec. Publ.* **1984**, *16*, 77–94. [CrossRef]
149. Bloomer, S.; Taylor, B.; MacLeod, C.J.; Stern, B.; Fryer, P.; Hawkins, J.W.; Jhonson, L. Early arc volcanism and the ophiolite problem: A perspective from drilling in the Western Pacific. *Act. Margins Marg. Basins West. Pac.* **1995**, *88*, 1–30.
150. Stern, R.J.; Morris, J.; Bloomer, S.H.; Hawkins, J.W., Jr. The source of metasomatic fluids and the generation of arc melt: Trace element and radiogenic isotope evidence from Eocene boninites, Mariana forearc. *Geochim. Cosmochim. Acta* **1991**, *55*, 1467–1481. [CrossRef]
151. Kimura, J.I.; Nakajima, J. Behaviour of subducted water and its role in magma genesis in the N.E. Japan arc: A combined geophysical and geochemical approach. *Geochim. Cosmochim. Acta* **2014**, *143*, 165–188. [CrossRef]
152. Plank, T.; Kelley, K.A.; Zimmer, M.M.; Hauri, E.H.; Wallace, P.J. Why do mafic arc magmas contain ~4% water on average? *Earth Planet. Sci. Lett.* **2013**, *364*, 168–179. [CrossRef]
153. Jackson, E.D. Chemical variation in coexisting chromite and olivine in chromitite zones of the Stillwater Complex. *Econ. Geol. Monogr. Ser.* **1996**, *4*, 41–71.
154. Fabries, J. Spinel-olivine geothermometry in peridotites from ultramafic complexes. *Contrib. Mineral. Petrol.* **1979**, *69*, 329–336. [CrossRef]
155. Engi, M.; Evans, B.W. Contributions to Mineralogy and A Re-Evaluation of the Olivine-Spinel Geothermometer: Discussion. *Contrib. Mineral. Petrol.* **1980**, *73*, 201–203. [CrossRef]
156. Jaques, A.L.; Green, D.H. Anhydrous melting of peridotite at 0–15 kb pressure and the genesis of tholeiitic basalts. *Contrib. Miner. Petrol.* **1980**, *73*, 287–310. [CrossRef]
157. Deng, X.H.; Chen, Y.J.; Santosh, M.; Yao, J.M. Genesis of the 1.76 Ga Zhaiwa Mo–Cu and its link with the Xiong'ervolcanics in the North China Craton: Implications for accretionary growth along the margin of the Columbia supercontinent. *Precambrian Res.* **2012**, *227*, 337–348. [CrossRef]

158. Bédard, J.H. Petrogenesis of boninites from the Betts Cove Ophiolite, Newfoundland, Canada: Identification of subducted source components. *J. Petrol.* **1999**, *40*, 1853–1889. [CrossRef]
159. Cooper, L.B.; Plank, T.; Arculus, R.J.; Hauri, E.H.; Hall, P.S.; Parman, S.W. High-Ca boninites from the active Tonga Arc. *J. Geophys. Res. Solid Earth* **2010**, *115*. [CrossRef]
160. Falloon, T.J.; Danyushevsky, L.V.; Ariskin, A.; Green, D.H.; Ford, C.E. The application of olivine geothermometry to infer crystallization temperatures of parental liquids: Implications for the temperatures of MORB magmas. *Chem. Geol.* **2007**, *241*, 3–4. [CrossRef]
161. Stern, R.J.; Bloomer, S.H. Subduction zone infancy: Examples from the Eocene Izu–Bonin–Mariana and Jurassic California Arcs. *Geol. Soc. Am. Bull.* **1992**, *104*, 1621–1636. [CrossRef]
162. Weaver, B.L.; Tarney, J. The Scourie dyke suite: Petrogenesis and geochemical nature of Proterozoic subcontinental mantle. *Contrib Mineral Petrol* **1981**, *78*, 175–178. [CrossRef]
163. Sheraton, J.W.; Black, L.P.; McCulloch, M.T.; Oliver, R.L. Age and origin of a compositionally varied mafic dyke swarm in the Bunger Hills, East Antarctica. *Chem Geol* **1990**, *85*, 215–246. [CrossRef]
164. Pal, T.; Ghosh, B.; Chakraborty, S. Petrogenesis of Archaean chromite deposits of the Roro-Jojohatu areas in the Singhbhum craton: A Boninitic parental melt in suprasubduction zone setting. *J. Geol. Soc. India* **2008**, *72*, 635–647.
165. Mir, A.R.; Alvi, S.H.; Balaram, V. Boninitic geochemical 1262 characteristics of high-Mg mafic dykes from the Singhbhum Granitoid Complex, eastern India. *Chin. J. Geochem.* **2015**, *34*, 241–251. [CrossRef]
166. Mukherjee, R.; Mondal, S.K.; Rosing, M.T.; Frei, R. Compositional variations in the Mesoarchean chromianspinels of the Nuggihalli schist belt, Western Dharwar Craton (India): Potential parental melts and implications for tectonic setting. *Contrib. Miner. Petrol.* **2010**, *160*, 865–885. [CrossRef]
167. Naqvi, S.M.; Khan, R.M.K.; Manikyamba, C.; Mohan, M.R.; Khanna, T.C. Geochemistry of the Neoarchaean high-Mg basalts, boninites and adakites from the Kushtagi–Hungund greenstone belt of the eastern Dharwar craton (EDC); implications for the tectonic setting. *J. Asian Earth Sci.* **2006**, *27*, 25–44. [CrossRef]
168. Jayananda, M. Geochemical constraints on komatiite volcanism from Sargur Group Nagamangala greenstone belt, western Dharwar craton, southern India: Implications for Mesoarchean mantle evolution and continental growth. *Geosci. Front.* **2013**, *4*, 321–340.
169. Jayananda, M.; Kano, T.; Peucat, J.J.; Channabasappa, S. 3.35 Ga komatiite volcanism in the western Dharwar craton, southern India: Constraints from Nd isotopes and whole rock geochemistry. *Precamb. Res.* **2008**, *162*, 160–179. [CrossRef]
170. Maya, J.M.; Bhutani, R.; Balakrishnan, S.; Sandhya, S.R. Petrogenesis of 3.15 Ga old Banasandra komatiites from the Dharwar craton, India: Implications for early mantle heterogeneity. *Geosci. Front.* **2016**, *8*, 467–481. [CrossRef]
171. Manikyamba, C.; Kerrich, R.; Khanna, T.C.; Krishna, A.K.; Satyanarayanan, M. Geochemical systematics of komatiite–tholeiite and adakitic - arc basalt associations: The role of a mantle plume and convergent margininformationof the SandurSuperterrane, Dharwar craton, India. *Lithos* **2008**, *106*, 155–172. [CrossRef]
172. Manikyamba, C.; Kerrich, R.; Polat, A.; Saha, A. Geochemistry of two stratigraphicallyrelated ultramafic (komatiite) layers from the Neoarchean Sigegudda greenstone terrane, western Dharwar craton, India: Evidence for compositional diversity in Archean mantle plumes. *Lithos* **2013**, *177*, 120–135. [CrossRef]
173. Malviya, V.P.; Arima, M.; Pati, J.K.; Kaneko, Y. Petrology and geochemistry of metamorphosed basaltic pillow lava and basaltic komatiite in the Mauranipur area: Subduction related volcanism in the Archean Bundelkhand craton, Central India. *J. Mineral. Petrol. Sci.* **2006**, *101*, 199–217. [CrossRef]
174. Balaram, V.; Singh, S.P.; Satyanarayanan, M.; Anjaiah, K.V. Platinum group elements geochemistry of ultramafic and associated rocks from Pindar in Madawara igneous complex, Bundelkhand massif, Central India. *J. Earth System Sci.* **2013**, *122*, 79–91. [CrossRef]
175. Habtoor, M.A.; Ahmed, A.H.; Akizawa, N.; Harbi, H.; Arai, S. Chemical homogeneity of high-Cr chromitites as indicator for widespread invasion of boninitic melt in mantle peridotite of Bir Tuluha ophiolite, Northern Arabian Shield. Saudi Arabia. *Ore Geol Rev.* **2017**, *90*, 243–259. [CrossRef]
176. Ahmed, A.H.; Arai, S.; Attia, A.K. Petrological characteristics of the Pan African podiform chromitites and associated peridotites of the Proterozoic ophiolite complexes, Egypt. *Miner. Depos.* **2001**, *36*, 72–84. [CrossRef]